Nat Hazards
DOI 10.1007/s11069-016-2692-3

ORIGINAL PAPER

Modeling coastal tsunami hazard from submarine mass failures: effect of slide rheology, experimental validation, and case studies off the US East Coast

Stéphan T. Grilli[1] · Mike Shelby[1] · Olivier Kimmoun[2] · Guillaume Dupont[2] · Dmitry Nicolsky[3] · Gangfeng Ma[4] · James T. Kirby[5] · Fengyan Shi[5]

Received: 12 August 2016 / Accepted: 18 November 2016

Abstract We perform numerical simulations to assess how coastal tsunami hazard from submarine mass failures (SMFs) is affected by slide kinematics and rheology. Two types of two-layer SMF tsunami generation models are used, in which the bottom (slide) layer is depth-integrated and represented by either a dense Newtonian fluid or a granular flow, in which inter-granular stresses are governed by Coulomb friction (Savage and Hutter model). In both cases, the upper (water) layer flow is simulated with the non-hydrostatic 3D σ-layer model NHWAVE. Both models are validated by simulating laboratory experiments for SMFs made of glass beads moving down a steep plane slope. In those, we assess the convergence of results (i.e., SMF motion and surface wave generation) with model parameters and their sensitivity to slide parameters (i.e., viscosity, bottom friction, and initial submergence). The historical Currituck SMF is simulated with the viscous slide model, to estimate relevant parameters for simulating tsunami generation from a possible SMF sited near the Hudson River Canyon. Compared to a rigid slump, we find that deforming SMFs of various rheology, despite having a slightly larger initial acceleration, generate a smaller tsunami due to their spreading and thinning out during motion, which gradually makes them less tsunamigenic; the latter behavior is controlled by slide rheology. Coastal tsunami hazard is finally assessed by performing tsunami simulations with the Boussinesq long wave model FUNWAVE-TVD, initialized by SMF tsunami sources, in nested grids of increasing resolution. While initial tsunami elevations are very large (up to 25 m for the rigid slump), nearshore tsunami elevations are significantly reduced in all

✉ Stéphan T. Grilli
grilli@egr.uri.edu

[1] Department of Ocean Engineering, University of Rhode Island, Narragansett, RI 02882, USA

[2] IRPHE, Ecole Centrale de Marseille, 13013 Marseille, France

[3] Geophysical Institute, University of Alaska Fairbanks, Fairbanks, AK 99775, USA

[4] Department of Civil and Environmental Engineering, Old Dominion University, Norfolk, VA 23529, USA

[5] Department of Civil Engineering, Center for Applied Coastal Research, University of Delaware, Newark, DE 19716, USA

Published online: 01 December 2016

cases (to a maximum of 6.5 m). However, at most nearshore locations, surface elevations obtained assuming a rigid slump are up to a factor of 2 larger than those obtained for deforming slides. We conclude that modeling SMFs as rigid slumps provides a conservative estimate of coastal tsunami hazard while using a more realistic rheology, in general, reduces coastal tsunami impact.

Keywords Tsunami propagation · Landslides · Rheology · Coastal geohazard · Boussinesq and non-hydrostatic wave models

1 Introduction

1.1 General context

As evidenced by the catastrophic 2004 Indian Ocean (IO; e.g., Grilli et al. 2007; Ioualalen et al. 2007) and 2011 Tohoku (TO), Japan (Grilli et al. 2013; Tappin et al. 2014), events, megatsunamis can devastate the world's increasingly populated coastal areas, causing high fatalities (over 200,000 for the IO tsunami and over 18,000 for the TO tsunami), destroying fragile coastal infrastructures, and imposing enormous loss to the economy of the most impacted countries (e.g., an over $300B loss due to the TO tsunami impact in Japan; WRAPUP-2 2011). Commensurate with their catastrophic impact, the IO and TO coseismic events were associated with the third and fifth largest earthquakes ever witnessed in human history ($M_w \sim 9.3$, Grilli et al. 2007; and $\sim$9.1, Grilli et al. 2013, respectively), which caused large seafloor deformation in close proximity to the Indonesian and Japanese coastline, respectively (in the Andaman subduction zone (SZ) and Japan Trench (JT), respectively). Hence, tsunami propagation times to these shores were short (15–25 min), reducing warning times, and coastal impact was maximized as there was no time or space for horizontal wave energy spreading to occur, leading to extreme run-ups of over 40 m at some locations.

Despite the large earthquake magnitude, studies of the TO tsunami showed that another mechanism/source was needed to explain the highest run-ups observed along the 80-km Sanriku coast, north of the main rupture area (e.g., Fujii et al. 2011; Satake et al. 2013; Wei et al. 2014, by performing waveform inversion; e.g., Grilli et al. 2013, by performing direct simulations). While new seismically related mechanisms were proposed (e.g., Romano et al. 2012), Tappin et al. (2014) showed that observations could be explained by additional waves generated by a very large ($\sim$500 km^3) rigid slump, triggered with some delay by the earthquake near the trench, in a 3000–4000 m depth, north of the main rupture. This was consistent with the many large historical slumps found in the JT area, and geological/geotechnical data and analyses.

Although less catastrophic to society, at least to modern society, than that associated with the TO event, large tsunamis have been triggered by SMFs or subaerial slides in the distant to recent past. While it is not our purpose to present their exhaustive list, we will point out a few events deemed important, either due to their size, induced tsunami/run-up, or simply the debate they caused in the literature, such as the 24–50 ky BP 134–165 km^3 Currituck SMF (Locat et al. 2009; Geist et al. 2009; Grilli et al. 2015a), 8150 BP 3500 km^3 Storegga subaerial slide (Harbitz 1992), 200 km^3 1929 Grand Bank SMF (Pipe et al. 1999; Fine et al. 2005), 40 km^3 1946 Unimak SMF (Watts and Grilli 2003; Fryer et al.

2004; Von Huene et al. 2014), 0.03 km^3 1958 Lituya Bay subaerial slide (Fritz et al. 2001; Weiss et al. 2009), 0.027 km^3 1975 Kitimat subaerial slide (Murty 1979; Kirby et al. 2016), and 0.0003 km^3 1994 Skagway subaerial slide (Fine et al. 1998) (see also the review of historical SMFs by Harbitz et al. (2013), for additional cases and a discussion).

An increasing body of work has been devoted to studying these historical cases, many of which occurred as highly deforming debris flows, to elucidate and model the underlying SMF mechanisms. However, studies of SMF tsunamis really intensified following the seminal 1998 Papua New Guina (PNG) event (e.g., Tappin et al. 2001, 2008). Here, a moderate M_w 7.1 earthquake, which should not have been significantly tsunamigenic, had apparently triggered a very large tsunami that caused a 15-m inundation on the Sissano spit, killing over 2200 people in the process. In view of this conflicting evidence, a large number of field and numerical studies were conducted, which showed that the earthquake had triggered a sizable (about 6 km^3) underwater slump, with a 15-min delay, 1600 m deep off of the Sissano Spit, whose waves were responsible for the large inundation and run-up focused on the spit (Tappin et al. 2008). This event was perhaps the first well-documented case supporting the large tsunamigenic and destructive potential of SMF tsunamis, leading to a large number of follow-up studies and developments of theoretical/numerical models (e.g., Grilli and Watts 1999, 2005; Watts et al. 2003, 2005; Grilli et al. 2002, 2010a; Lynett and Liu 2002, 2005; Ataie-Ashtiani and Najafi-Jilani 2006, 2007; Ataie-Ashtiani and Shobeyri 2008; Fernández-Nieto et al. 2008; Løvholt et al. 2008; Abadie et al. 2008, 2010; Fuhrman and Madsen 2009; Weiss et al. 2009; Horrillo et al. 2013; Ma et al. 2013, 2015; Yavari-Ramshe and Ataie-Ashtiani 2015; for details, see the very exhaustive review by Yavari-Ramshe and Ataie-Ashtiani 2016) and laboratory experiments (e.g., Fritz et al. 2001, 2004; Enet et al. 2003; Enet and Grilli 2007; Grilli and Watts 2005; Liu et al. 2005; Ataie-Ashtiani and Najafi-Jilani 2008; Ataie-Ashtiani and Nik-khah 2008; Najafi-Jilani and Ataie-Ashtiani 2008; Heller and Hager 2010; Mohammed and Fritz 2012; Viroulet et al. 2014; McFall and Fritz 2016). PNG 1998 also led to the reanalysis of past events that also had conflicting evidence and whose tsunami generation might have been associated with SMF. For instance, Fryer et al. (2004) reanalyzed the 1946 Unimak event in view of new field data and found evidence for a large SMF, but could not be fully conclusive regarding tsunami generation. The more recent and detailed surveys by Von Huene et al. (2014) confirmed the presence of a 40-km^3 block that had slid a large vertical distance; as a result, new modeling of this event is in progress.

Past volcanic eruptions have also been associated with the generation of large and destructive tsunamis, from pyroclastic flows and/or caldera collapse, such as the 1883 Krakatau (e.g., Maeno and Imamura 2011) or more recently the 2002 Stromboli (Tinti et al. 2005), eruptions. Additionally, fast-growing young volcanoes periodically suffer large mass failures associated with partial to total flank collapse, which have large tsunamigenic potential. This has been well documented for the Hawaii volcanoes by Moore et al. (1989) and the Canary Islands volcanoes (in particular the Cumbre Vieja Volcano (CVV) on La Palma) by McMurtry et al. (2007) (for instance, they estimated that the latest large scale collapse of the CVV may have occurred 250 ka ago). In a recent study of the Fogo volcano on Cape Verde island, Ramalho et al. (2015) showed that a catastrophic flank collapse may have occurred 73 ka ago, as at least one fast voluminous event that triggered tsunamis of enormous height and energy, causing over 270-m run-up on the nearby Santiago island. In more recent history, in 1888, a 5-km^3 flank collapse of Ritter Island (Papua New Guinea) produced damaging tsunami waves at distances of up to 500 km; the resulting landslide removed most of the subaerial Ritter Island, reducing the 800-m-high edifice to a crescent-shaped remnant (Ward and Day 2003; Day et al. 2015). In

1975, a M7.2 earthquake struck the Big Island of Hawaii in Kalapana, causing a tsunami that created a 7- to 14-m run-up on the nearby shores. In a detailed study, Day et al. 2005 showed that a slump motion of a large part of the Kilauea volcano southeast flank (with a 7200 km^3 volume) was likely responsible for a large part of the observed near-field tsunami. Finally, in 1980, the eruption of Mount St Helens caused a 2.5-km^3 rockslide-debris avalanche (Glicken 1996).

As shown by Tappin et al. (2014), large SMFs can potentially be triggered by megathrust earthquakes and contribute additional waves to tsunami generation; as they concluded, this has important implications for assessing coastal hazard from future megathrust events. However, as also seen above, there are many historical precedents for significant tsunamis being generated by large SMFs, which may have only required a small earthquake to be triggered. Hence, for some coastlines with moderate seismicity, such as the United States (US) East Coast, it is believed that near-field SMF tsunamis may be one of the dominant sources of coastal tsunami hazard (Grilli et al. 2015a, b and next section); hence, improving their modeling, particularly with respect to SMF rheology and mechanism, is important for proper tsunami hazard assessment. This paper aims at making a step in this direction.

1.2 Specific context (USEC)

Besides scientific interest, the main motivation for this work is to better assess coastal tsunami hazard from SMFs located off of the US East Coast (USEC), along the Atlantic Ocean margin and shelf slope. In this context, since 2009, as part of the US National Tsunami Hazard Mitigation Program (NTHMP; http://nthmp.tsunami.gov/index.html), the US-based authors have been developing inundation maps for the USEC, through numerical modeling. (NTHMP was created in 1995, in the wake of the devastating IO tsunami.) To date, such maps have been based on envelopes of coastal inundation caused by plausible maximum tsunamis (PMTs) in the considered oceanic basin. In the Atlantic Ocean basin, PMTs were identified from a variety of geological processes (or sources), including (ten Brink et al. 2008, 2014; Grilli et al. 2015b): (i) far-field coseismic sources, such as a M9 earthquake in the Puerto Rico Trench (PRT) (e.g., Grilli et al. 2010b), or a M8.9 earthquake in the Açores Convergence Zone (ACZ), similar to the 1755 Lisbon earthquake (e.g., Barkan et al. 2009); (ii) a large volcanic collapse of the CVV in the Canary Islands (e.g., Løvholt et al. 2008; Abadie et al. 2012; Tehranirad et al. 2015); and (iii) near-field SMFs near the mainly siliciclastic continental shelf break (e.g., Grilli et al. 2009, 2015a, b; Chaytor et al. 2009; ten Brink et al. 2008, 2009a, b; Schnyder et al. 2016). Improving the modeling of these SMF sources and their potential impact on the USEC are the main goal of this work, in particular estimating effects of slide rheology on coastal tsunami hazard.

While few historical tsunamis caused by SMFs were clearly identified to have impacted the USEC (e.g., the 1929 Grand Bank tsunami; Fine et al. 2005; Piper et al. 1999), ten Brink et al. (2008, 2009a, b, 2014), Chaytor et al. (2009), and Twichell et al. 2009 mapped numerous paleo-SMFs, whose total surface area covered a significant portion of the USEC continental slope and rise, with many of these being of large volume (tens to over 100 km^3). In recent history, the USEC only experienced a moderate seismicity, up to M7.2, but this was sufficient to trigger a 200-km^3 debris flow and a damaging tsunami in the Grand Banks in 1929 (Fine et al. 2005). Studies of other historical SMFs, such as the 1998 PNG, confirmed that this level of seismicity is sufficient to trigger large SMFs and cause catastrophic tsunamis. Specific studies of the

tsunamigenic potential of SMFs off of the USEC have shown that these may pose the largest tsunami hazard among PMTs in the Atlantic basin (ten Brink et al. 2008, 2009a, b; Grilli et al. 2009, 2015a). In particular, to identify the location of future tsunamigenic SMFs, Grilli et al. (2009) performed Monte Carlo simulations (MCS) of SMFs triggered by seismicity along the USEC, in which stochastic slope stability analyses were run for thousands of SMFs with randomly selected parameters, along many cross-shore transects from Florida to Cape Cod, MA. North of Virginia, the MCS predicted a 500-year run-up of up to 5–6 m, which is commensurate with the largest impact from other PMTs (Grilli et al. 2015b). South of Virginia, the MCS predicted a significantly reduced run-up. In view of these results, Grilli et al. (2015a) performed additional geophysical and geotechnical analyses and selected 4 areas where large tsunamigenic SMFs could occur, due to high seismicity combined with large bottom slopes and a sufficient accumulation of sediment (Fig. 1). One large SMF was then parameterized and its tsunami generation modeled in each area, using the characteristics of the largest historical failure in the region, the 134- to 165-km^3 Currituck slide complex (Fig. 1); these were referred to as SMF Currituck proxy sources.

Currituck is the largest paleo-SMF identified along the western Atlantic Ocean margin and occurred between 24 and 50 ka ago, in a period when sea level was much lower. This event has been extensively studied from the geological and slide triggering points of view (e.g., Locat et al. 2009, and references herein). Tsunami generation from a reconstituted Currituck SMF was first studied by Geist et al. (2009), using a simplified SMF tsunami

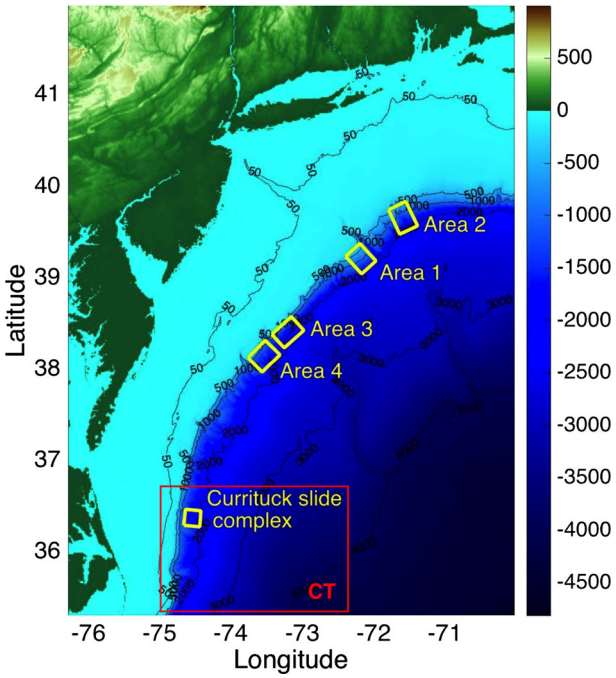

Fig. 1 Location of areas 1–4 identified by Grilli et al. (2015a), off of the upper USEC, as having high potential for large tsunamigenic SMFs (from Shelby et al. 2016). The *red box* marks the boundary of the 500-m-resolution NHWAVE Cartesian grid CT used to simulate the Currituck SMF motion (see Table 1). Depth is in meters, in the *color scale* and bathymetric contours

generation model. Before simulating the SMF Currituck proxies in areas 1–4, Grilli et al. (2015a) modeled tsunami generation and coastal impact for the historical Currituck slide. Similar to the methodology used by Tappin et al. (2014) to simulate a dual coseismic-rigid slump (SMF) source for the TO tsunami, they used the non-hydrostatic three-dimensional (3D) (σ layer) model NHWAVE (Ma et al. 2012) to simulate tsunami generation and, once waves were generated and slump motion ended, they propagated the tsunami in a series of nested grids of increasingly fine resolution toward the coast, using the two-dimensional (2D) fully nonlinear and dispersive Boussinesq long wave model FUNWAVE-TVD (Shi et al. 2012; Kirby et al. 2013). The SMF law of motion and geometry were specified as bottom boundary conditions in NHWAVE (also see Grilli and Watts 1999, 2005; Watts et al. 2005; Enet and Grilli 2007; Grilli et al. 2010a). In the bathymetry provided to NHWAVE, they recreated the unfailed slope, by assuming the SMF had a quasi-Gaussian profile with an elliptical footprint. To maximize tsunami generation, as suggested by Grilli and Watts (2005), they modeled the SMF kinematics as a rigid slump, using Locat et al.'s (2009) estimate of the SMF center of mass maximum velocity. Results showed that, with the present sea level, the Currituck slide would have generated a large tsunami, causing significant inundation (over 5 m) in the area of Norfolk, VA, and south of it, as well as along the shores of the Delmarva peninsula, including Ocean City, MD. Following the same methodology, Grilli et al. (2015a) then modeled tsunami generation from the SMF Currituck proxies sited in areas 1–4 (Fig. 1), assuming they behaved as rigid slumps. The computed coastal inundation and run-up were finally included in the corresponding NTHMP inundation maps.

Earlier experimental and numerical work concluded that tsunami generation from SMFs primarily depends on their initial acceleration (which depends on seafloor slope and SMF shape/added mass) and volume, and to a lesser extent on their failure mechanism (e.g., slump or slide) and rheology (i.e., rigid or deforming) (e.g., Watts et al. 2003, 2005; Grilli and Watts 2005; Ataie-Ashtiani and Najafi-Jilani 2008; Najafi-Jilani and Ataie-Ashtiani 2008; Tappin et al. 2008; Geist et al. 2009; Grilli et al. 2009; Yavari-Ramshe and Ataie-Ashtiani 2016). Watts and Grilli (2003) and Grilli and Watts (2005), for instance, showed that a SMF with moderate (arbitrary) deformation generated a slightly smaller tsunami, with a reduced coastal hazard. Running 2D simulations of deforming slides with a Bingham fluid model (BING; Imran et al. 2001), Watts and Grilli (2003) concluded that the slide center of mass kinematics was not affected by slide deformation. Ataie-Ashtiani and Najafi-Jilani (2008) and Najafi-Jilani and Ataie-Ashtiani (2008) experimentally showed that granular slides had a maximum amplitude up to 15% smaller than that of the equivalent rigid slide, and a period 10% longer. Other factors that increase coastal tsunami hazard from SMFs, whether rigid or deforming, are: (i) an initially shallow submergence, enhancing tsunami generation (in fact the initial surface depression and energy transfer from slide to water motion; Ataie-Ashtiani and Najafi-Jilani 2008); (ii) a location at a short distance from shore, reducing energy spreading (and warning times); and (iii) a more directional and focused wave generation, causing larger inundation along a narrow section of the coast. As the continental shelf is wide along the upper USEC, where large SMFs are more likely to occur (areas 1–4; Fig. 1), items (i) and (ii) are less likely to be important for SMF tsunami hazard; this would be different along the US West Coast, which is bordered by a narrow shelf.

In this study, in view of recent progress made, we revisit the modeling of SMF tsunami generation and coastal impact on the USEC, in the context of the SMF Currituck proxy approach, to estimate the effect of slide rheology on tsunami hazard. As indicated above, earlier work concluded that a moderate SMF deformation should generally result in a

slightly reduced tsunami generation and coastal hazard. However, in some situations, local bathymetry, 3D effects, seafloor properties, and SMF geometry could significantly affect slide kinematics and tsunami generation, in a manner that should be quantified through proper modeling. Additionally, assuming that all SMFs behave as rigid slumps is both unrealistic and can be too conservative in many cases. Hence, for the purpose of developing both realistic and accurate inundation maps for NTHMP, or other similar tsunami hazard assessment program, it is important to apply the latest and most appropriate SMF models. Accordingly, in this paper, we first summarize the equations and methods for two recent deforming SMF models developed by some of the authors. Both models have a two-layer domain, with the upper water layer being modeled with NHWAVE and the SMF being a depth-integrated bottom layer assumed to be: either (i) a dense Newtonian fluid (Kirby et al. 2016), or (ii) a saturated granular medium in which inter-granular stresses are governed by Coulomb friction (Savage and Hutter model; Ma et al. 2015). Both models are then validated and benchmarked against recent laboratory experiments performed for SMFs, made of small glass beads, moving down a plane slope. The dense fluid model (note the granular model is not yet applicable to an arbitrary bathymetry) is then applied to simulate tsunami generation from the historical Currituck slide and the SMF Currituck proxy in area 1; results for slide motion and tsunami generation are compared with those of the same SMFs modeled as rigid slumps. We then draw some conclusions regarding tsunami hazard assessment.

2 Numerical models and modeling methodology

2.1 Overview

A variety of numerical models have been proposed to simulate tsunami generation by SMFs or subaerial slides, particularly since the 1998 PNG event, which was caused by a deep SMF moving as a rigid slump (e.g., Tappin et al. 2001, 2008); an overview of these models was given in introduction. While we do not intend to make an exhaustive review of SMF tsunami models, in the following, we give a brief list of such models that have been used to simulate tsunami generation: (1) by rigid SMFs or subaerial slides, by specifying their geometry and motion as a bottom boundary conditions, with the fluid motion being modeled based on: (i) potential flow theory (e.g., Grilli and Watts 1999, 2005; Watts et al. 2005; Grilli et al. 2002), (ii) dispersive long wave equations (e.g., Lynett and Liu 2002, 2005; Tinti et al. 2005; Ataie-Ashtiani and Najafi-Jilani 2007, 2008; Fuhrman and Madsen 2009), or (iii) Navier–Stokes/Euler equations (e.g., Assier-Rzadkiewicz et al. 1997; Liu et al. 2005; Ataie-Ashtiani and Shobeyri 2008; Abadie et al. 2008, 2010; Ma et al. 2012; Horrillo et al. 2013; Viroulet et al. 2013; Grilli et al. 2015a); and (2) by deforming SMFs or subaerial slides, based on: (i) coupled depth-integrated (non-dispersive) equations for both the slide and coupled fluid motion, assumed to be a dense Newtonian or Bingham fluid (e.g., Jiang and LeBlond 1992; Jiang and Leblond 1993; Heinrich 1992; Fine et al. 1998, 2005) or a granular flow (Savage–Hutter type; e.g., Iverson and Denlinger 2001; Fernández-Nieto et al. 2008), (ii) Navier–Stokes equations for both slide and fluid (e.g., Harbitz 1992; Harbitz et al. 1993; Assier-Rzadkiewicz et al. 1997; Ataie-Ashtiani and Shobeyri 2008; Løvholt et al. 2008; Abadie et al. 2008, 2010, 2012; Weiss et al. 2009; Horrillo et al. 2013; Ma et al. 2013), and (iii) on a depth-integrated dense fluid or granular flow layer (Savage–Hutter type) for the SMF coupled to 3D Navier–Stokes/

Euler equations for the fluid flow (Ma et al. 2015; Kirby et al. 2016). For details, see the exhaustive review by Yavari-Ramshe and Ataie-Ashtiani (2016).

It should be pointed out that, in some of these models, the fluid flow, i.e., the generated SMF tsunami, is simulated with non-dispersive equations (i.e., with a model neglecting vertical accelerations or non-hydrostatic pressures). The inclusion of frequency dispersion in tsunami models has been shown by many authors to be necessary for an accurate modeling of SMF tsunami generation and propagation. Essentially, this is due to the typically smaller wavelength to depth ratio of SMF tsunami waves as compared to coseismic tsunami waves (see, e.g., Grilli and Watts 1999, 2005; Watts and Grilli 2003; Tappin et al. 2008; Ma et al. 2012; Horrillo et al. 2013; Glimsdal et al. 2013). Failing to include dispersive/non-hydrostatic effects in the model used to simulate SMF tsunami generation has been shown to cause large errors on the shape and kinematics of initial waves (e.g., Tappin et al. 2008; Ma et al. 2012). Likewise, failing to include dispersion in the model used to propagate the highly dispersive wave trains that are typically generated, has been shown to cause additional errors in wave height and steepness (and hence coastal impact), due to the inaccurate simulation of constructive/destructive wave–wave interactions during propagation. Without the inclusion of dispersion, the simulated landslide tsunami waves will thus be limited to one or two leading waves and lack the long oscillatory tail observed experimentally (see the many experimental works listed before), in the field (e.g., Tappin et al. 2014), or numerically (e.g., Watts et al. 2003; Tappin et al. 2008; Løvholt et al. 2008; Abadie et al. 2012; Tehranirad et al. 2015; Grilli et al. 2015a).

Hence, in this work, tsunami generation by SMFs is modeled with the 3D non-hydrostatic (i.e., dispersive) model NHWAVE (Ma et al. 2012), which uses a horizontal Cartesian grid and a boundary fitted σ-coordinate grid in the vertical direction. Once the tsunami is fully generated and has evolved into a long wave train, wave propagation and coastal impact are simulated with the 2D fully nonlinear and dispersive long wave Boussinesq model FUNWAVE-TVD (Shi et al. 2012; Kirby et al. 2013), in a series of nested grids of increasingly fine resolution toward shore (see, e.g., Grilli et al. 2013, 2015a, b; Tappin et al. 2014; Tehranirad et al. 2015, for more details on this approach). Using different models for SMF tsunami generation and propagation is typical in operational landslide tsunami hazard assessment, in part due to the variety of temporal and spatial scales involved (e.g., Watts et al. 2003; Day et al. 2005; Tappin et al. 2008, 2014; Løvholt et al. 2008; Abadie et al. 2012; Horrillo et al. 2013), and leads to more accurate and efficient simulations than using a 3D model, such as NHWAVE, with a regular grid throughout.

For rigid SMFs, tsunami generation is simulated in NHWAVE following the methodology detailed in Grilli et al. (2015a), in which the SMF law of motion (slump or slide) and geometry are specified as bottom boundary conditions (see also Grilli and Watts 2005; Watts et al. 2005; Enet and Grilli 2007). For deforming SMFs, tsunami generation is simulated using NHWAVE's most recent two-layer model, in which the SMF is represented as a bottom layer, made of either a dense fluid (Kirby et al. 2016) or a saturated granular medium of the Savage–Hutter type, in which inter-granular stresses are governed by Coulomb friction (Ma et al. 2015), whose motion is coupled with that of the water in the upper layer along the deforming SMF–water interface. While the upper layer is fully 3D, as in the standard NHWAVE model, in both cases, the SMF equations of mass and momentum conservation are depth-integrated in the bottom layer, similar to those obtained in a long wave generation model, and include volumetric and bottom friction dissipation terms. When simulating laboratory experiments, the actual initial shape of the SMF is modeled, whereas in field case studies, the rigid or deforming SMF geometry is modeled as

an initial sediment mound of quasi-Gaussian cross sections, with an elliptical footprint over the slope (see Enet and Grilli 2007; Grilli et al. 2015a for details).

While deforming SMFs can fail with a large variety of failure modes and rheology (e.g., Hungr et al. 2001), both models used here, as well as those listed above, approximate the geological complexity of SMF failure by an idealized depth-integrated flow model, such as a dense Newtonian or Bingham fluid model or a granular flow model (Savage and Hutter model; e.g., Iverson and Denlinger 2001). The main justification for this is that, as discussed in introduction, both experimental and numerical sensitivity studies have shown that tsunami generation is, to the first-order, governed by the SMF initial acceleration, volume, and depth, with additional smaller, second-order, effects of SMF deformation and rheology. Deformation causes an increase in the SMF initial acceleration, which increases tsunami generation, and a decrease in thickness over time, which decreases tsunami generation, both acting at the same time. With these competing effects, while SMF shape may be strongly affected by deformation, in general, tsunami amplitude will be much less affected (as shown, e.g., in Ataie-Ashtiani and Najafi-Jilani's 2008; Najafi-Jilani and Ataie-Ashtiani's 2008, experiments). Some early two-layer tsunami generation long wave models (e.g., Jiang and LeBlond 1992; Jiang and Leblond 1993) emphasized slide deformation and used a complex slide rheology (such as Bingham), implying that deformation itself is fundamentally tsunamigenic. However, in such models, deformation may appear to have significant effects because the shallow water approximation causes the free surface to closely follow the motion of the slide–water interface during tsunami generation. Watts and Grilli (2003), based on simulations with BING, concluded that it may not be necessary for proper tsunami generation to use a complex deforming slide rheology (such as Bingham's), but instead a more sophisticated wave generation model is needed, particularly one that includes frequency dispersion; neglecting the latter effects in tsunami generation in fact in general causes much larger errors than those associated with a simplified rheology, particularly late in the slide motion. The present work is consistent with these conclusions, in which the upper water layer is modeled by 3D Euler equations (with NHWAVE) and the bottom slide layer is modeled with a depth-integrated, dense Newtonian fluid or granular flow, layer.

In the next section, we first validate the two deforming SMF models against laboratory experiments for tsunami generation by SMFs made of glass beads moving down a plane slope. Field case studies are considered next. However, only the model with a dense fluid layer will be used for those, because the granular model cannot yet simulate an arbitrary bathymetry with depth $h(x, y)$ (the extension to an arbitrary bathymetry is in progress). Below, we recall the governing equation only for the dense fluid slide layer, and the reader is invited to consult the references for additional details and information, particularly regarding numerical implementation and methods.

2.2 Two-layer NHWAVE models

Two types of two-layer models are used in this work (Fig. 2), in which the upper water layer is modeled with the 3D non-hydrostatic model NHWAVE (Ma et al. 2012) and, following Jiang and LeBlond (1992), Jiang and Leblond (1993), and Fine et al. (2008), the motion of the bottom slide layer is based on depth-integrated equations (for both mass and momentum conservation) and modeled either as a dense Newtonian fluid (Kirby et al. 2016) or a granular flow (Savage and Hutter model) (Ma et al. 2015). When considering the many types of deforming SMFs that can occur (e.g., Hungr et al. 2001), the first type of model should be better suited to simulate mudflows, while the second type of model should

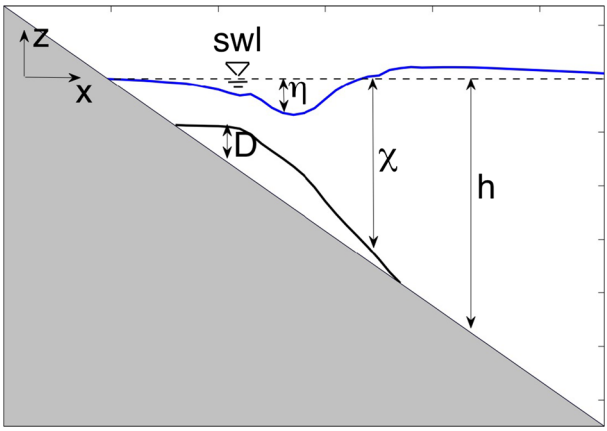

Fig. 2 Sketch of a vertical cross section in Kirby et al.'s (2016) deforming slide model, with definition of key geometric parameters

better apply to granular and debris flows. However, as discussed above, the accurate modeling of tsunami generation and coastal hazard are the main goal of this work. In this respect, the center of mass motion of deforming slides is quite close to that of rigid slides, particularly for small times, and tsunami generation depends more on slide initial acceleration, volume, and submergence, and on the proper inclusion of dispersive effects in the wave model, than on details of slide deformation. Hence, while using a more complex flow model, such as Bingham in the dense fluid case may improve the modeling of slide shape (in particular its bulbous front), this should not significantly affect tsunami generation. Likewise, while the second type of two-layer models should be more relevant for simulating the laboratory experiments performed for glass beads (see next section), both types of two-layer models will be benchmarked using these experiments, focusing on wave generation, which is more central to this study.

For the model with a dense fluid layer (Kirby et al. 2016), the governing equations of the bottom layer read,

$$\begin{aligned} \frac{\partial \mathbf{D}}{\partial t} + \nabla_h \cdot \mathbf{F} &= \varepsilon \nabla_h^2 D, \\ \frac{\partial \mathbf{F}}{\partial t} + \frac{6}{5}\nabla_h \cdot \left(\frac{\mathbf{F}\mathbf{F}}{D}\right) &= -gD\left\{-\frac{\rho_s - \rho_w}{\rho_s}\nabla_h \chi + \frac{\rho_w}{\rho_s}\nabla_h \eta\right\} \\ &\quad - \frac{\mu}{\rho_s}\left\{3\frac{\mathbf{F}}{D^2} - \nabla_h^2 \mathbf{F}\right\} - \frac{g n^2}{D^{1/3}}\frac{\mathbf{F} \mid \mathbf{F} \mid}{D^2}, \end{aligned} \tag{1}$$

where $\mathbf{F} = (DU, DV)$ with $D = h - \chi$ (where h is the fixed bathymetry without the slide, i.e., the substrate), χ denotes the distance from the still water level (swl) to the slide interface (Fig. 2), $\mathbf{U} = (U, V)$ is the depth-averaged horizontal velocity vector (directions x and y), $\nabla_h = (\partial/\partial x, \partial/\partial y)$ is the horizontal gradient operator, ρ_w and ρ_s are the water and slide bulk density, respectively, μ is the slide (dense fluid) dynamic viscosity, g is gravitational acceleration, and n is the Manning coefficient for the slide–substrate bottom friction. The right-hand side of the first Eq. (1) is introduced for numerical regularization purpose, with ε being chosen such that conservation of slide volume is ensured (see Kirby et al. 2016). Terms in the right-hand side of the second Eq. (1) represent the pressure gradient due to both the slide–water interface and free surface slopes, (viscous) dissipation

within the slide, and bottom friction dissipation at the slide–substrate interface, respectively. Note that Eq. (1) is expressed in the Cartesian horizontal axes (x, y) and assumes that the slide layer is thin compared to the scale of along slope variation, similar to a typical long wave equation model for which horizontal scales are assumed to be larger than vertical scales; hence, this also leads to assuming a mild slope and neglecting vertical accelerations as compared to gravity. For steeper slopes, however, such as in the laboratory experiments presented hereafter, the vertical acceleration term may no longer be negligible.

While the actual physics of basal friction associated with landslides is much more complex than described by a standard bottom friction force, with a constant Manning's roughness coefficient (e.g., Viesca and Rice 2010, 2012; Yavari-Ramshe and Ataie-Ashtiani 2015), and may include the possibility of hydroplaning (e.g., Blasio et al. 2004), we shall see that a model based on the simple depth-integrated Eq. (1) can accurately simulate tsunami generation by deforming SMFs and be parameterized (by the proper calibration of μ and n) to reproduce the salient features of the SMF (e.g., kinematics, runout, thickness), although details (such as a bulbous front) will be missing.

In field case studies, as indicated before, once the SMF has stopped moving or is too deep to be tsunamigenic (for time $t > t_f$) (whether rigid or deforming), computations are continued in FUNWAVE-TVD, which has both Cartesian coordinates, fully nonlinear (Shi et al. 2012), and spherical coordinates, weakly nonlinear (Kirby et al. 2013), implementations. To do so, surface elevation $\eta(x,y)$ and horizontal velocity $\mathbf{U}(x,y)$ computed in NHWAVE are interpolated on FUNWAVE-TVD's first level grid (for the velocity this is done at the required depth $0.531h$ to achieve extended dispersion properties; Shi et al. 2012), as an initial condition, and simulations are restarted and pursued by one-way coupling, in a series of nested grid of increasingly fine resolution and commensurately accurate bathymetric and topographic data toward the coast (e.g., Grilli et al. 2013, 2015a, b; Tehranirad et al. 2015). The one-way coupling method works as follows: Time series of surface elevation and depth-averaged velocity are computed at a large number of stations/numerical wave gages, defined in a coarser grid, along the boundary of the finer grid used in the next level of nesting. Computations are fully performed in each coarser grid and then are restarted in the next level of finer grid, using the station time series as boundary conditions. As these include both incident and reflected waves computed in the coarser grid, the coupling method closely approximates open boundary conditions. It was found in earlier work that a nesting ratio with a factor 3–4 reduction in mesh size achieved good accuracy in tsunami simulations. Note that to prevent reflection in the first grid level, sponge layers are used along all the offshore boundaries (see details in Shi et al. 2012). For each grid level, whenever possible, bathymetry and topography are interpolated from data of accuracy commensurate with the grid resolution. Along the USEC, in deeper water, we use NOAA's 1-arc-min resolution ETOPO-1 data; in shallower water and on the continental shelf, we use NOAA's NGDC 3" and 1" Coastal Relief Model data. Typically, the weakly nonlinear spherical implementation is used over larger deeper-water grids, whereas the Cartesian fully nonlinear model is used over smaller, high-resolution, nearshore nested grids.

The rationale for the two model approach is that: (i) FUNWAVE cannot currently simulate waves generated by a moving bottom; (ii) NHWAVE can simulate a moving bottom for a rigid SMF and has been extended to include a deforming slide layer (Ma et al. 2015; Kirby et al. 2016); (iii) Being 3D, NHWAVE can more accurately simulate SMF tsunami generation in deeper water (i.e., for more dispersive waves), during which velocities can be much more non-uniform over depth than during subsequent tsunami

Fig. 3 Setup for laboratory experiments of tsunami generation by underwater slides made of glass beads performed in the Ecole Centrale de Marseille (IRPHE) precision tank of (useful) length $l = 6.27$ m, width $w = 0.25$ m, and water depth $h = 0.330$ m. Upon release, beads are moving down a $\theta = 35$ degree slope. **a** Longitudinal cross section with marked location of sluice gate and 4 wave gages (WG1, WG2, WG3, WG4). **b**, **c** Zoom-in on side and cross-sectional views of slope and sluice gate (dimensions marked in mm). **d** Picture of experimental setup around slope and sluice gate

propagation (see, e.g., Grilli et al. 2002); (iv) In its fully nonlinear implementation, FUNWAVE-TVD is more accurate than NHWAVE for simulating coastal wave transformations and impact, in particular, regarding the moving shoreline algorithm; (v) Although both models are heavily and efficiently parallelized, FUNWAVE-TVD is more computationally efficient as it is only 2D, and hence uses grids at least 3 times smaller than the minimum NHWAVE grid with 3 σ-layers that provides a similar approximation of horizontal velocities in the vertical direction; and finally, (vi) FUNWAVE-TVD also has a spherical implementation, which allows a more accurate simulation of far-field tsunami propagation. Note, in the present applications, because all simulations will be performed in regional or nearshore grids with small latitudinal and longitudinal ranges, spherical coordinates will not be necessary, although combinations of spherical and Cartesian nested grids have been used in earlier work with FUNWAVE-TVD (see, e.g., Grilli et al. 2013, 2015a, b; Kirby et al. 2013).

3 Experimental validation of deforming slide models

3.1 Description of laboratory experiments and results

Laboratory experiments of tsunami generation by underwater slides made of glass beads were performed at the Ecole Centrale de Marseille (IRPHE), France, in a precision tank of (useful) length $l = 6.27$ m and width $w = 0.25$ m (Fig. 3). In each experiment, a Mass W_b of beads of density $\rho_b = 2500\,\mathrm{kg/m^3}$ was submerged in fresh water of density $\rho_w = 1000\,\mathrm{kg/m^3}$, in a reservoir of triangular shape located on a $\theta = 35°$ slope, fronted by a sluice gate. Experiments were started by withdrawing the gate into a bottom cavity within the slope (using a highly repeatable motion controlled by springs, visible in Fig. 3d), which takes about 0.125 s. Fifty-eight experiments were performed with each experiment being repeated twice (i.e., there were 29 individual sets of parameters). Independent parameters set in experiments were the tank water depth, set to $h = 0.320$–0.370 m, the glass bead diameter, set to either $d_b = 4$ or 10 mm and their total dry weight, set to $W_b = 1.5$–2.5 kg. In 20 experiments, a thin layer of glass beads was glued on the slope while glass beads were free to slide in other experiments. Each experiment was recorded using a high-speed video camera (at 1000 frames per s) set on the side of the tank, showing both the underwater motion of the beads and the resulting free surface deformation (Fig. 4). In each experiment, time series of free surface elevations were measured at 4 capacitance or resistive wave gages WG1–WG4 (Fig. 3a), $\eta_i(t)$ $(i = 1, 2, 3, 4)$.

Figure 4 shows snapshots extracted from the video taken during one of the landslide tsunami experiments, with parameters: $h = 0.330$ m, $d_b = 4$ mm, $W_b = 2$ kg, and no glued beads on the slope. In Fig. 4a, glass beads are initially stored in a triangular reservoir with the sluice gate up; the start time of the experiment, $t = 0$, corresponds to the withdrawing of the gate into the bottom cavity, slightly before (Fig. 4b). Once free to move, the glass beads slide down the slope and their motion creates an initial depression

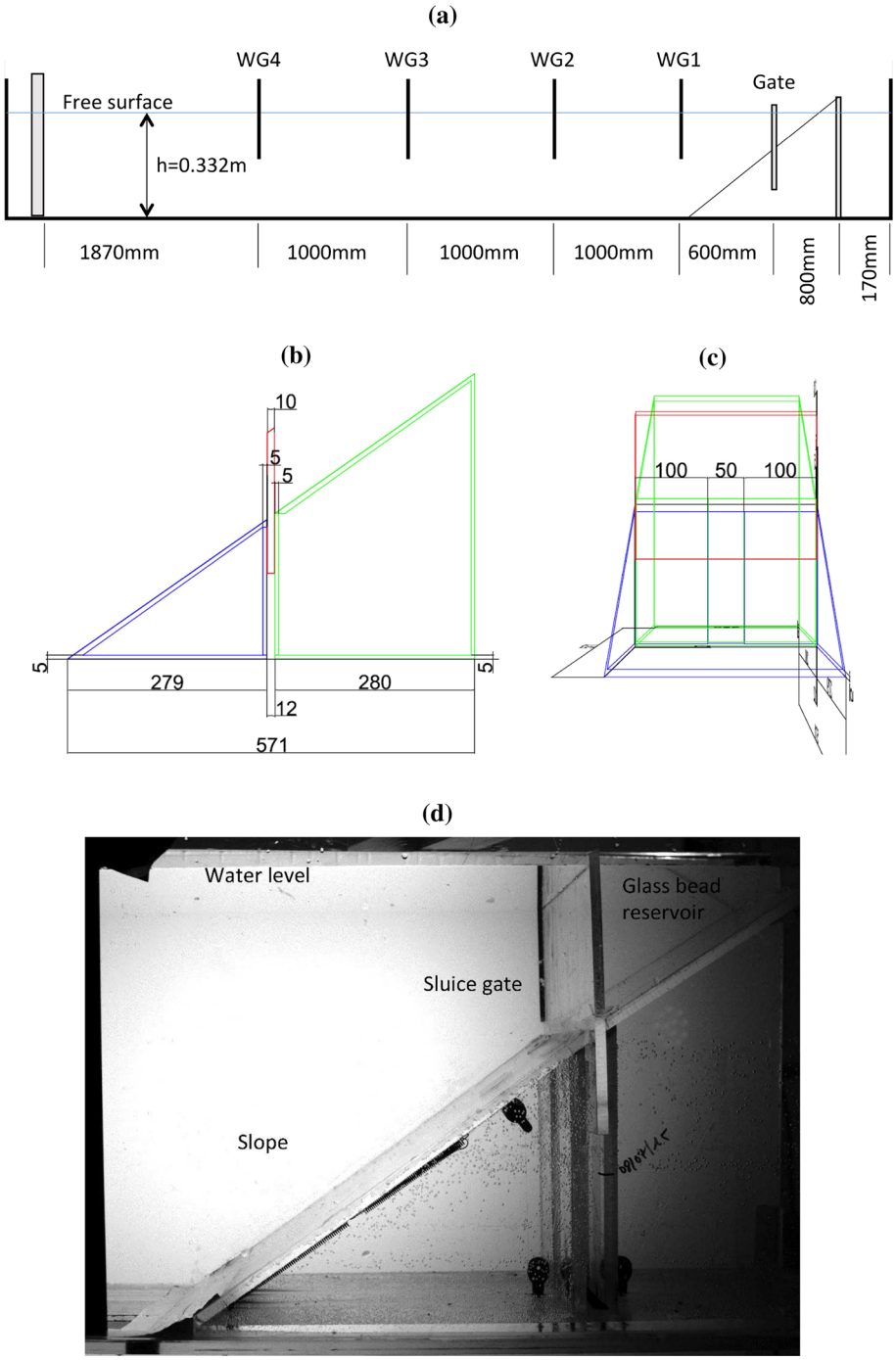
(a)
WG4
WG3
WG2
WG1
Gate
Free surface
h=0.332m
1870mm
1000mm
1000mm
1000mm
600mm
800mm
170mm
(b)
10
5
5
5
279
280
5
12
571
(c)
100
50
100
(d)
Water level
Glass bead reservoir
Sluice gate
Slope

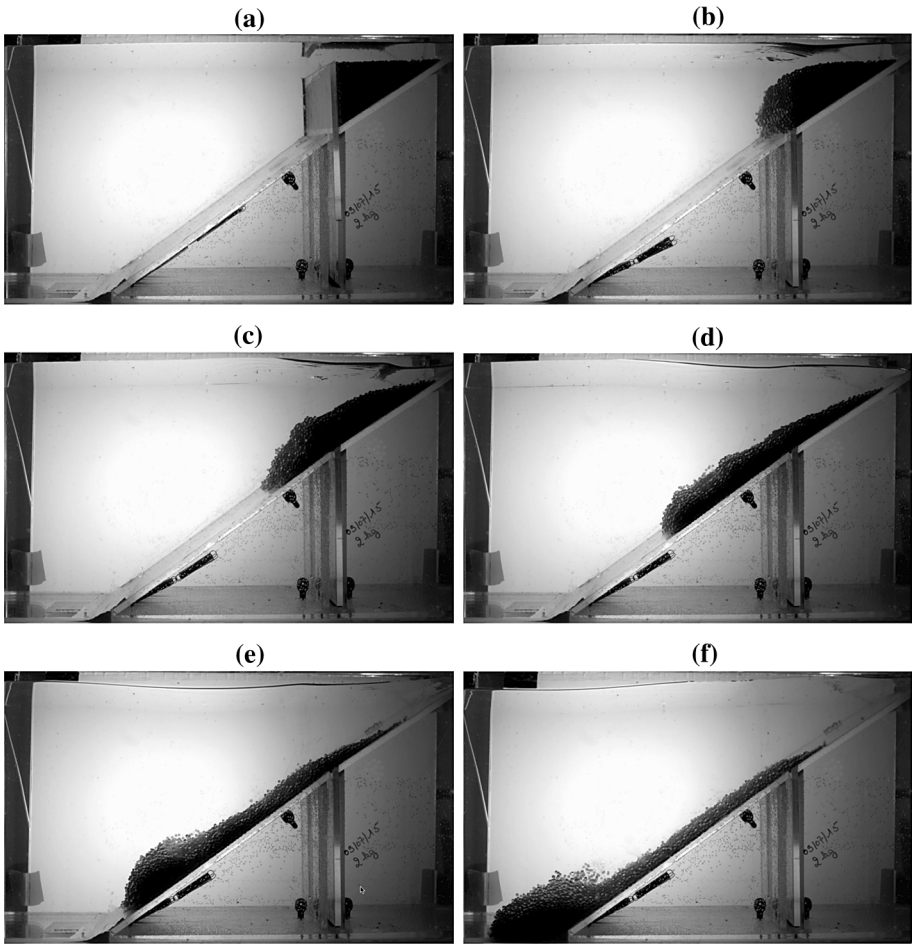

Fig. 4 Snapshots of laboratory experiments of tsunami generation by underwater slides made of glass beads (Fig. 3), for $h = 0.330$ m, $d_b = 4$ mm, $W_b = 2$ kg, and no glued beads on the slope, at times t = **a** −0.125, **b** 0.02, **c** 0.17, **d** 0.32, **e** 0.47, and **f** 0.62 s. Glass beads are initially stored within a triangular reservoir, with the sluice gate up; once the gate has withdrawn into its cavity (t = 0), the deforming slide moves down the 35°. slope causing free surface deformation

of the water surface (Fig. 4b), which then rebounds, creating two sets of waves moving down and up the tank (Fig. 4c). The "onshore" moving waves cause run-up on the slope, while the "offshore" moving waves reflect on the far end of the tank and propagate back toward the generation area (Fig. 4d–f). This behavior is also clearly seen in time series measured at wave gages WG1–WG4 (Fig. 5). Measurements showed that this and other experiments are highly repeatable, with almost unnoticeable differences between wave gage measurements for two replicates of the same experiment. More details of the experimental setup and methods and of results of the 58 experiments will be reported elsewhere.

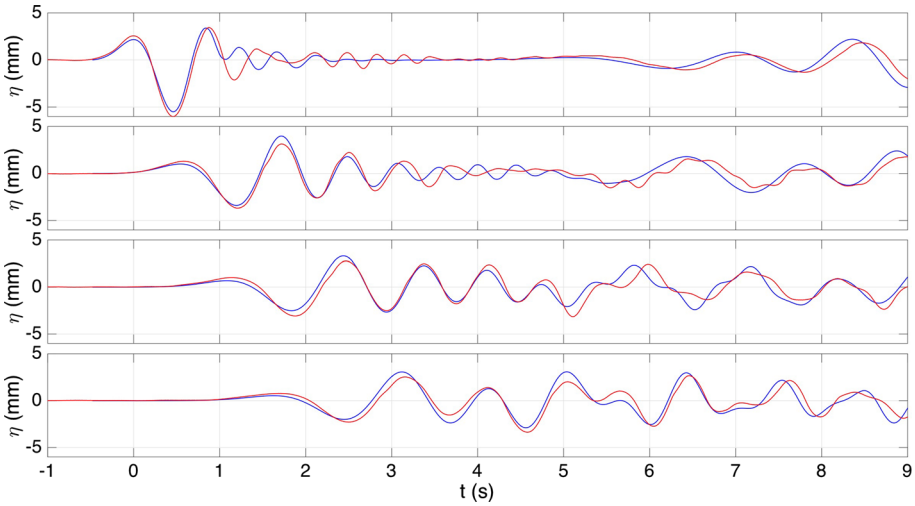

Fig. 5 Comparison of observed (*blue*) time series of surface elevation at wave gages WG1 to WG4 (Fig. 3a), from *top* to *bottom*, to those computed (*red*) using NHWAVE, with a dense Newtonian fluid layer underneath with: $\rho_s = 1951$ kg/m^3, $\mu_s = 0.01$ kg/(m s) and $n = 0.04$. The model (base) grid uses $\Delta x = \Delta y = 0.01$ m horizontally and 9 σ-layers in the vertical direction. Note, the origin of the time axis corresponds to the arrival of the first elevation wave at gage WG1.

3.2 Numerical modeling of laboratory experiments

We benchmark the two two-layer models detailed above, with either a dense Newtonian fluid sublayer (Kirby et al. 2016) or a saturated granular medium sublayer (Ma et al. 2015), by simulating a single representative glass bead experiment corresponding to the case and parameters of Fig. 4: $h = 0.330$ m, $d_b = 4$ mm, $W_b = 2$ kg, and no glued beads on the slope. In this simulation, the entire tank geometry is modeled in NHWAVE, starting from the situation shown just before the stage of Fig. 4b when the gate has just withdrawn ($t = 0$). Numerical wave gages are located in the model at the same locations as shown in Fig. 3a and simulated time series are compared with experiments.

To apply the granular flow model, we simply define a granular material made of spherical grains of density and diameter identical to the glass beads used in experiments. To apply the dense fluid model, however, we first need to estimate the fluid density ρ_s equivalent to the initial mixture of glass beads and water. Also, because only the diameter d_b and total dry weight of glass beads W_b were measured in experiments, for both models, we need to compute the location of the resting interface between slide and water (Fig. 4a), i.e., the initial slide submergence h_s, whose value significantly affects tsunami generation (Grilli and Watts 2005). Finally, for both models, we need to specify realistic values of the Manning bottom friction coefficient n and the parameter controlling the volumetric energy dissipation. For the dense fluid, the latter is the dynamic viscosity μ_s and for the granular medium it is the internal Coulomb friction angle φ_{int} and dynamic bed friction angle φ_{bed}, plus a calibration parameter λ controlling the pore pressure and friction near the bed. (For instance, to simulate Heller and Hager's 2000 2D granular slide experiments, Ma et al. 2015 used $\varphi_{int} = 34°$ and $\varphi_{bed} = 24°$).

While the maximum regular packing of spheres is $\phi_m = \pi/(3\sqrt{2}) = 74.0\%$ of the volume occupied by the spheres, studies of randomly packed spheres yield packing values

typically near (and bounded by) $\phi = 63.4\%$ (Song et al. 2008). Here, we will use this value, meaning that for a saturated medium, $1 - \phi = 36.6\%$ of voids are filled with water. Hence, the equivalent fluid density for modeling the slide as a dense fluid is: $\rho_s = (1-\phi)\rho_w + \phi\rho_b = 1951$ kg/m^3. Slide volume is then found as, $V_s = W_s/(\phi\rho_b) = 1.262 \times 10^{-3}$ m^3, and the initial front thickness of the slide is derived from the triangular geometry of the glass bead reservoir (Figs. 3, 4a) as, $T = \sqrt{2\tan\theta\, V_s/w} = 0.084$ m. Based on the dimensions shown in Fig. 3b, we finally find the initial slide submergence for the considered experiment as, $h_s = h - T - 0.291\tan\theta = 0.0422$ m.

For the dense fluid model, assuming the suspension of water with a high concentration of glass beads behaves as a Newtonian fluid, theoretical expressions have been proposed for $\eta_r = \mu_s/\mu$ (with μ the suspending fluid viscosity),

$$\eta_r = \left(1 + \frac{1.25\,\phi}{\left(1 - \frac{\phi}{\phi_m}\right)}\right)^2, \quad \frac{9}{8}\left(\frac{\left(\frac{\phi}{\phi_m}\right)^{\frac{1}{3}}}{1 - \left(\frac{\phi}{\phi_m}\right)^{\frac{1}{3}}}\right), \text{ and } \quad \left(1 - \frac{\phi}{\phi_m}\right)^{-2} \tag{2}$$

by Eilers (1941), Frankel and Acrivos (1967), and Quemada (1977), respectively. (For details regarding theoretical developments and experimental validations of these expressions, see Mendoza and Santamara-Holek 2009; Mueller et al. 2010). Hence, for the above values of ϕ and ϕ_m, Eqs. (2) yields $\eta_r = 42.7$, 21.3, and 48.9, respectively. Assuming the dynamic viscosity of fresh water is $\mu = 0.001$ kg/(m s), these equations predict $\mu_s \in$ [0.0213–0.0489] kg/(m s). Just after the initiation of motion (e.g., Fig. 4b), the slide still has nearly the maximum random packing density ϕ and, hence, using a viscosity in this range is a reasonable assumption. However, as the slide deforms and moves down the slope (Fig. 4c–d), the glass bead volume fraction decreases, which based on Eq. (2) causes the equivalent slide density and viscosity to decrease. To account for this, in the dense fluid model, we used a lower value of viscosity, $\mu_s = 0.01$ kg/(m s). Additionally, using a lower value of viscosity can help compensate for the nearly free slip of glass beads along the slope and the low bottom friction that results, when a layer of glass beads is not glued to the slope. A lower viscosity can also enhance the slide initial acceleration, which as indicated above, may be underestimated in the model Eq. (1). For this value of viscosity, a Manning coefficient $n = 0.04$ was calibrated so that the modeled slide reached the bottom of the slope at the time measured in experiments (Fig. 4).

For the granular flow model, friction parameters were first selected similar to those used by Heller and Hager's (2000), who modeled 2D experiments of granular slides, i.e., $\varphi_{int} = 34°$ and $\varphi_{bed} = 24°$, together with $\lambda = 0.5$ (note that a larger value of $\lambda \in [0, 1]$ will result in a reduced bed Coulomb friction). The "water on slide" or substrate friction coefficient was set to $C_f = 0$, as it was observed that its value did not significantly affect results. Then, to improve the agreement of the first generated wave with laboratory measurements, the internal friction was slightly adjusted to $\varphi_{int} = 41°$.

The selected glass bead experiment was modeled with both NHWAVE two-layer models, using the initial slide geometry computed above (T, h_s) and, for the dense fluid layer, the selected parameters, ρ_s, μ_s , and n, and for the granular flow model, the selected parameters, ρ_b, φ_{int}, φ_{bed}, λ, and C_f. A sensitivity analysis to grid resolution, detailed later, showed that results were well converged when using a horizontal grid resolution $\Delta x = \Delta y = 0.01$ m with 9 σ-layers in the vertical direction; this is referred to as the *base grid*.

Dense fluid model results. Figure 5 shows a comparison of time series of surface elevations computed in the base grid to those observed at the four wave gages WG1–WG4

(Fig. 3a). Overall, there is a good agreement of model results with the measurements, and more so for the incident wave train than for reflected waves, later in the time series, where discrepancies slightly increase, perhaps due to effects of far-end wall roughness in experiments, not represented in the model. More specifically, at gage WG1, the model reproduces well the 2 leading waves (i.e., first two crests and first trough), both incident and reflected, but shows increasing discrepancies for the smaller trailing waves; for the two leading incident waves, the root mean square (RMS) difference of the modeled $\eta_m(t)$ and experimental $\eta_e(t)$ surface elevations, scaled by the maximum wave height H_{max} (trough to crest) measured at each gage in experiments (here: 15.1, 11.7, 9.1, 10.4 mm, respectively): $\epsilon_{RMS} = \sqrt{\overline{(\eta_m - \eta_e)^2}}/H_{max} = 7.2\%$ (where the overbar denotes the mean). At gages WG2-WG4, due to dispersion, the two leading waves evolve into an increasing number of larger waves, which are all well simulated in the model (incident or reflected). We note that both the elevation and phase of waves are well simulated, indicating that dissipation in the slide and frequency dispersion effects during propagation are adequately modeled. The RMS error for the first three and four waves observed at gages WG2 and WG3, respectively, and, for the entire time series at gage WG4, is ϵ_{RMS} = 7.0, 6.6, and 8.4%, respectively.

Simulations of this experiment were repeated to study the sensitivity of model results to grid resolution. Thus, Fig. 6 shows results obtained using $\Delta x = \Delta y$ = 0.01 m m in the horizontal grid, with the number of σ-layers being 3, 6, or 9. The simulation with 3 σ-layers yields slightly lower values of crest and trough elevations, whereas results are nearly identical when using 6 or 9 σ-layers; 9 σ-layers will be used from now on. Figure 7 shows results using 9 σ-layers, with the horizontal grid resolution set to $\Delta x = \Delta y$ = 0.005, 0.01, or 0.02 m. A significant difference is observed when reducing the horizontal grid resolution from 0.02 to 0.01 m, and a much smaller difference is observed when further reducing the grid step to 0.005 m. Hence, results are deemed to have nearly converged for $\Delta x = \Delta y$ = 0.01 m and, for more efficiency, this resolution will be used from now on.

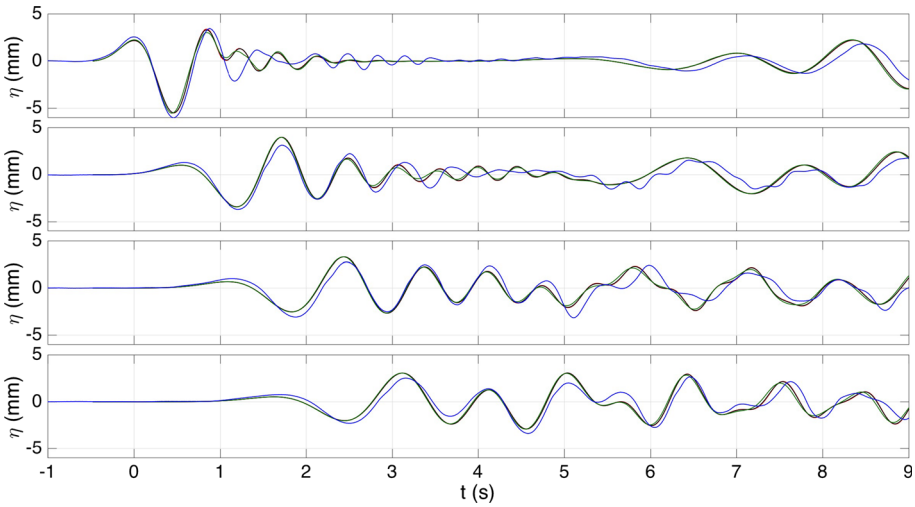

Fig. 6 Case of Fig. 5. Sensitivity of surface elevations computed at wave gages for $\Delta x = \Delta y$ = 0.01 m horizontally, to the number of σ-layers: 3 (*green*), 6 (*black*), and 9 (*red*), as compared to experimental data (*blue*)

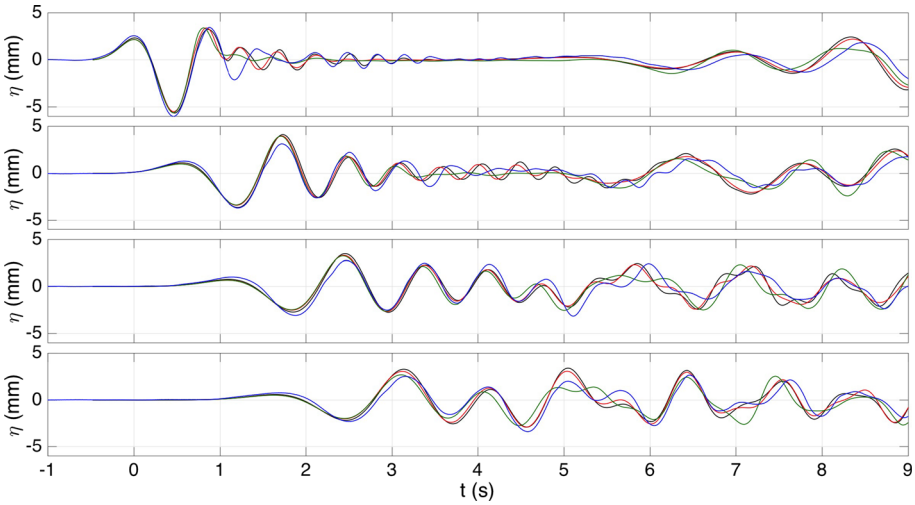

Fig. 7 Case of Fig. 5. Sensitivity of surface elevations computed at wave gages for 9 σ-layers, to the horizontal grid resolution, $\Delta x = \Delta y = 0.02$ (*green*), 0.01 (*red*), and 0.005 (*black*) m, as compared to experimental data (*blue*)

Figure 8 compares the slide cross sections computed at four times t = (a) 0.02, (b) 0.17, (c) 0.32, and (s) 0.47 s, to those observed in experiments with the high-speed camera. The magnitude of the computed flow velocity is also plotted in the figures as a color scale. A reasonable agreement is observed between the salient features of the computed and measured profiles, but clearly, this depth-integrated slide model does not reproduce the bulbous shape associated with a recirculating flow within the slide, that gradually develops at the front of the slide as time increases; as discussed before, however, this does not significantly affect wave generation as this part of the slide is no longer tsunamigenic. Also, Fig. 8a, b shows large changes in flow velocity over a small horizontal distance, between the near-initial stage at $t = 0.02$ s, and $t = 0.17$ s, indicating that the flow acceleration down the slope is large, with likely large associated vertical accelerations due to the steep slope. As indicated before, the latter are neglected in the slide model Eq. (1) and, although this does not appear to significantly affect the modeling of tsunami generation (as inferred from the good agreement in Fig. 5 of surface elevations at wave gages), including vertical accelerations in the slide model equations might further improve the agreement of the simulated and observed slide cross sections.

Granular flow model results. The same experiment was simulated with Ma et al.'s (2015) two-layer granular slide model, using the base grid discretization in NHWAVE, which ensures well converged results. As this model is still being developed and not yet applicable to arbitrary topography, the goal at this stage was only to verify that the model, which features more complete physics can accurately simulate the glass bead experiments. Once extended, this model will also be used in future work for coastal tsunami hazard assessment.

Figure 9 shows surface elevations computed at the four wave gage locations and compared to experiments. Numerical simulations appear to agree as well with experiments as results of the viscous slide model (see Fig. 5), particularly at gages WG2 to WG4, where the agreement with experiments even seems slightly better. At gage WG1 the agreement with experiments is less good and, from the small scale oscillations seen in the surface

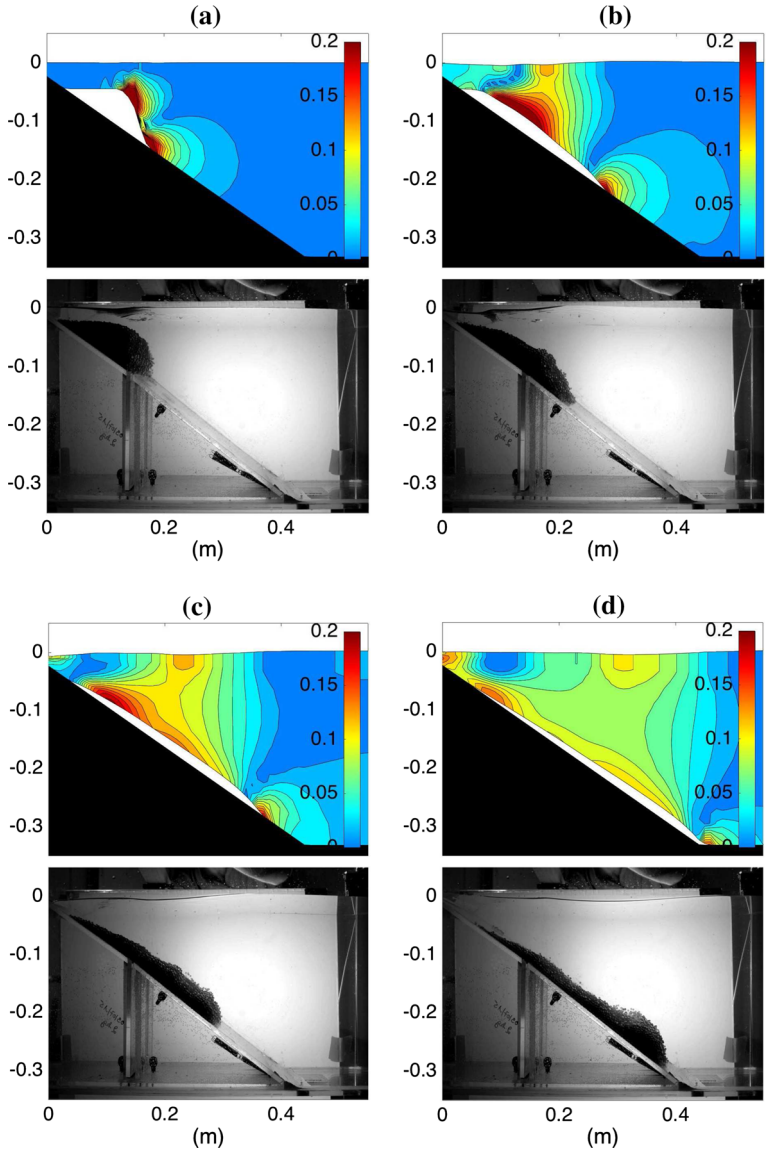

Fig. 8 Case of Fig. 5. Comparison of computed slide cross sections (*top*) with those observed in experiments with the high-speed camera (*bottom*), at times t = **a** 0.02, **b** 0.17, **c** 0.32, and **d** 0.47 s. *Color scales* are computed flow velocity modules in m/s

elevation, it appears that the granular flow model has greater difficulty representing the initially triangular geometry of the glass bead reservoir than the viscous slide model. Nevertheless, once generated, waves propagate down the tank and their elevation and wavelength (and hence phase speed), agree well with measurements at the other gages. These observations are consistent with the fairly small normalized RMS differences calculated, similarly to the viscous slide model, between observed and simulated surface elevations for the results of Fig. 9, as $\epsilon_{RMS} = 10.5$, 7.0, 6.4, and 7.7%, at gages WG1–

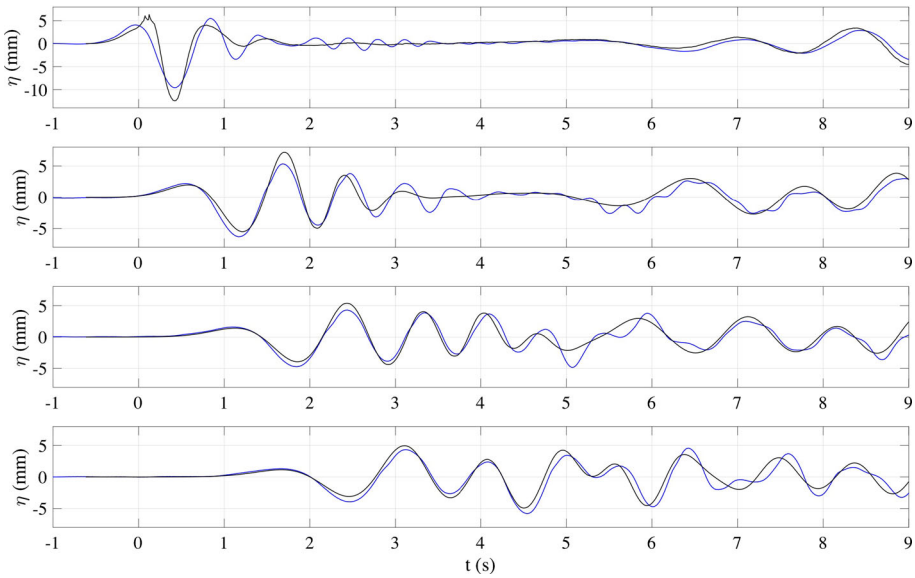

Fig. 9 Same case as Fig. 5. Comparison of observed (*blue*) time series of surface elevation at wave gages WG1 to WG4 (Fig. 3a), from top to bottom, to those computed using NHWAVE's granular flow model (*black*)

WG4, respectively; as expected from visual observation, ϵ_{RMS} is larger at gage WG1 and smaller at the other gages than for the dense fluid model.

3.3 Sensitivity of tsunami generation to slide rheology

Using the dense fluid model, we perform a sensitivity analysis of SMF tsunami generation to the model parameters related to slide rheology. For a Newtonian fluid, besides density, two parameters control the slide center of mass motion $S(t)$ down the slope (measured parallel to the slope): the equivalent slide viscosity μ_s and the Manning coefficient n; when these parameters are large, frictional dissipation increases, slowing down slide motion. Hence, when μ_s or n are increased in the model, once the slide picks up speed and friction forces become effective, we expect that slide acceleration and velocity will decrease, and also tsunami generation. For the initial part of slide motion down the slope, however, slide velocity is small and its motion should be close to that of a purely accelerating body, $S(t) \sim (A_o/2)\, t^2$, with A_o the initial acceleration parallel to the slope (Grilli and Watts 2005; Watts et al. 2005). Hence, one should not observe significant differences in slide motion and tsunami generation for small time, when changing μ_s or n.

These predictions are confirmed in Figs. 10 and 11, which show results of simulations corresponding to the case of Fig. 5, in which we first set the slide viscosity to μ_s = 1, 0.1, and 0.01 kg/(m s), with n = 0.04, and then set the slide–substrate Manning coefficient to n = 0.01, 0.04, and 0.07, with μ_s = 0.01 kg/(m s). In both figures, the computed slide center of mass motion $S(t)$, velocity $U(t) = \mathrm{d}S/\mathrm{d}t$, and acceleration $A(t) = \mathrm{d}U/\mathrm{d}t$ are plotted, together with the free surface elevations computed at gages WG1–WG4 (Fig. 3a), as compared to the experimental measurements. As expected, in both figures, for short times, $t < 0.1$ s or so, slide kinematics is not affected by the value of μ_s or n, consistent with this

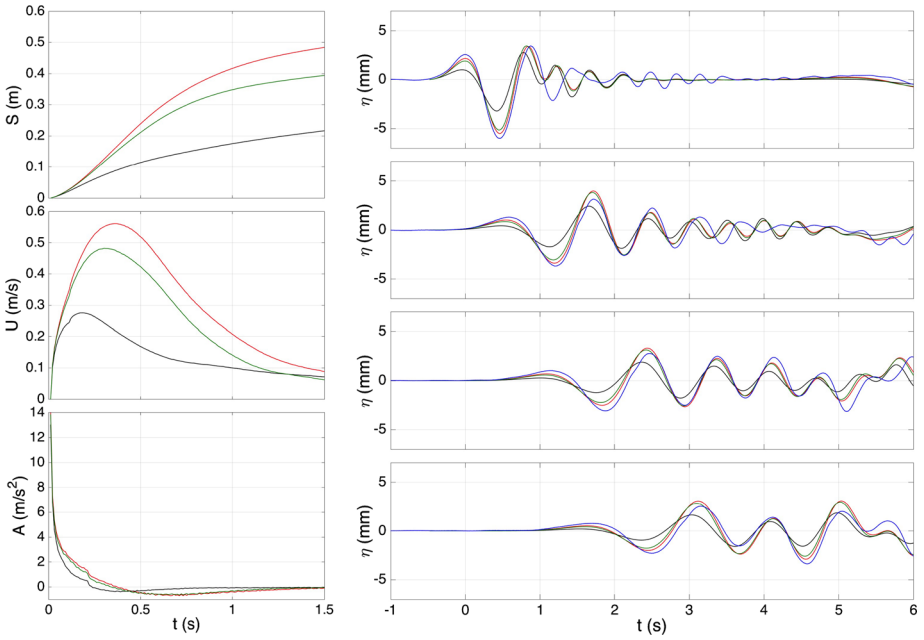

Fig. 10 Case of Fig. 5. Sensitivity of surface elevations computed at gages WG1–WG4 (Fig. 3a; *right panels* from *top* to *bottom*), as compared to experimental measurements (*blue*), to the equivalent slide viscosity μ_s = 0.01 (*red*), 0.1 (*green*), and 1 (*black*) kg/(m s), with n = 0.04. The *leftward* panels show the corresponding slide center of mass motion $S(t)$, velocity $U(t)$, and acceleration $A(t)$. Note, zero time for left panels is when the sluice gate has fully retracted, whereas for *right panels* it is when the first elevation wave reaches gage WG1

being a purely accelerating motion. For later times, however, while the bulbous slide front is still traveling down the slope (i.e., for $t < 0.5$ s or so; Fig. 4), both slide center of mass velocity and acceleration, and thus distance travelled by the slide on the slope in a given time, are reduced when μ_s or n are increased. Once the slide is on the flat bottom of the tank, this behavior may be slightly more complex. Results are also as expected regarding the free surface elevations modeled at wave gages, with a reduction in tsunami generation, as μ_s or n are increased.

3.4 Sensitivity of tsunami generation to slide submergence

Earlier numerical (e.g., Grilli and Watts 2005; Watts et al. 2005; Grilli et al. 2010a) and experimental (e.g., Enet et al. 2003; Enet and Grilli 2007; Grilli and Watts 2005; Liu et al. 2005; Ataie-Ashtiani and Najafi-Jilani 2008) work indicates that, all other parameters being equal, SMF tsunami generation increases when the SMF initial submergence depth h_s decreases. This was confirmed in simulations with the dense fluid model by re-running the experimental base case of Fig. 5, for a lower and a higher submergence, $h_s = 0.022$ and 0.062 m, respectively (with $\mu_s = 0.01$ kg/(m s) and n = 0.04); the latter was achieved by specifying a water depth, $h = 0.31$ and 0.35 m. Thus, Fig. 12 shows, as expected, that for the shallower submergence depth the largest leading trough and crest are significantly increased, as compared to the base case, particularly upon generation at gage WG1. For a

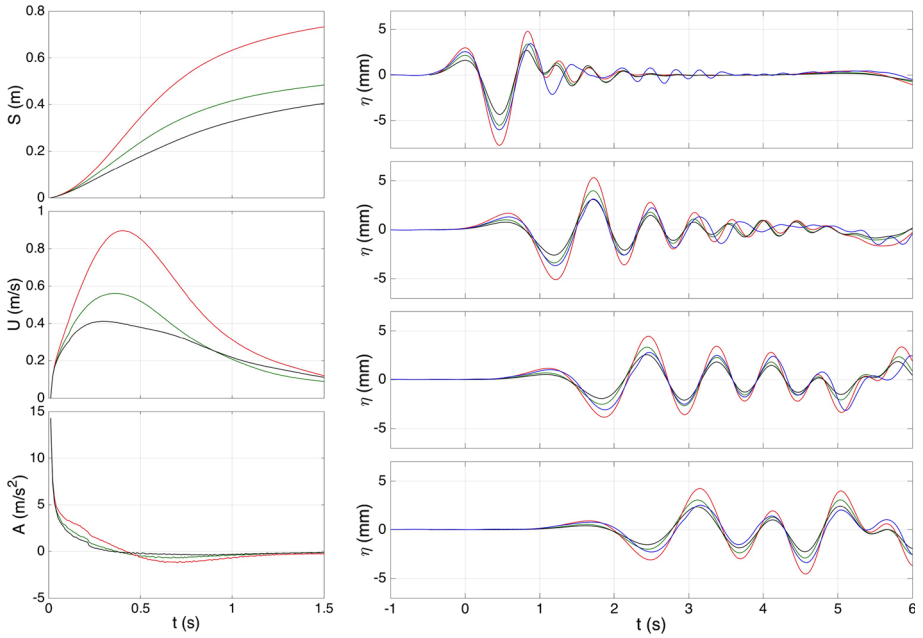

Fig. 11 Case of Fig. 5. Sensitivity of surface elevations computed at gages WG1–WG4 (Fig. 3a; *right panels* from *top* to *bottom*), as compared to experimental measurements (*blue*), to the slide–substrate Manning coefficient $n = 0.01$ (*red*), 0.04 (*green*), and 0.07 (*black*) kg/(m s), with $\mu_s = 0.01$ kg/(m s). The *leftward* panels show the corresponding slide center of mass motion $S(t)$, velocity $U(t)$, and acceleration $A(t)$. Note, zero time for left panels is when the sluice gate has fully retracted, whereas for *right panels* it is when the first elevation wave reaches gage WG1

larger submergence depth, the trend is opposite, but by a lesser amount, indicating that the dependence of maximum surface elevation to depth is nonlinear; this was already pointed out by Grilli and Watts (2005) and Enet and Grilli (2007) for rigid slides. At gages WG2–WG4, the same trends are preserved, but as dispersion distributes the changes in leading wave elevation to the trailing waves in the oscillatory tail, the effect of submergence depth is less marked than at the first gage.

Although these are complex processes, a simple physical interpretation for these results is that the deeper the slide on a plane slope, despite the same initial volume and acceleration, the smaller the initial depression the initial slide motion causes on the free surface and in turn the smaller the rebound waves that are generated. Once submergence becomes shallow enough, however, nonlinear effects that result from the larger wave amplitude-to-depth ratio cause an additional increase in wave elevation (similar to shallow water steepening).

4 Case studies off of the US East Coast

In the previous section, we assessed the accuracy of two two-layer models simulating tsunami generation by deforming SMFs, on the basis of laboratory experiments. Using the dense fluid model, we studied the result sensitivity to grid resolution, parameters governing

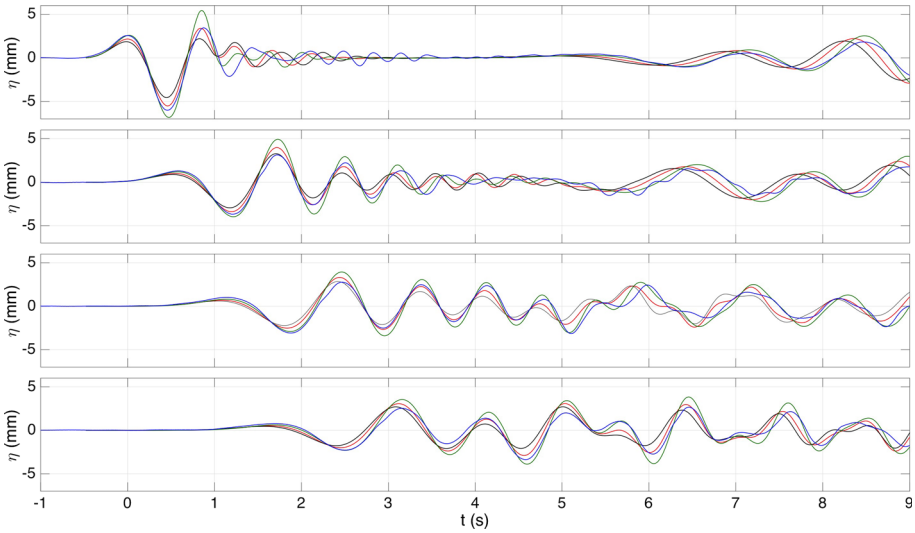

Fig. 12 Case of Fig. 5. Sensitivity of surface elevations computed at gages WG1–WG4 (Fig. 3a; *right panels* from *top* to *bottom*), as compared to experimental measurements (*blue*), to the slide initial submergence depth, $h_s = 0.022$ (*green*), 0.042 (*red*), and 0.062 (*black*) m, for a water depth $h = 0.31$ (*green*), 0.33 (*red*), and 0.35 (*black*) m, respectively, with $\mu_s = 0.01$ kg/(m s) and $n = 0.04$. Time is given in seconds after the initial crest reaches the first gage

fluid kinematics and rheology (i.e., equivalent slide viscosity μ_s and slide–substrate Manning friction coefficient n), and initial slide submergence h_s. In the following, we use the dense fluid model to simulate tsunami generation by deforming SMFs located off of the USEC, on the continental shelf break and slope, where SMF tsunami hazard was found to be highest (ten Brink et al. 2008, 2009a, b, 2014; Grilli et al. 2009; Chaytor et al. 2009). We evaluate effects of slide rheology on coastal tsunami hazard by comparing results to those obtained in our earlier simulations, in which SMFs were modeled as rigid slumps (Grilli et al. 2015a). Note that the granular slide model was not used to conduct these field case studies, because it is not yet applicable to an arbitrary bathymetry; this extension is currently being worked out. However, in the context of the USEC, where large historical slides such as Currituck have been shown to have failed more like debris flows with a large mud component (e.g., Prior et al. 1986; Locat et al. 2009; ten Brink et al. 2008, 2009b, 2014), using the dense fluid deforming slide model is likely more realistic.

As in earlier work, we model SMFs having the characteristics of the historical Currituck slide, i.e., "Currituck SMF proxies," located in area 1 in Fig. 1. Before performing this simulation, however, we revisit that of the historical Currituck slide, which was also modeled by Grilli et al. (2015a) as a rigid slump, by applying the deforming slide model, to estimate relevant values of μ_s and n that yield a slide center of mass motion, $S(t)$, similar to that of the earlier slump simulations, and hence a similar runout S_f after a main time of motion t_f. Using these parameters, we then perform simulations of the Currituck SMF proxy located in area 1, in the Hudson River canyon, and compare the generated tsunami and coastal impact to those previously obtained when modeling the SMF as a rigid slump.

4.1 Currituck slide complex

We simulate the historical Currituck slide motion using the deforming fluid-like slide model, in order to derive realistic values for the slide equivalent viscosity μ_s and Manning coefficient n, that yield a slide center of mass kinematics (i.e., maximum velocity and runout) similar to that of the rigid slump simulated earlier. Hence, we focus here on simulating slide motion rather than tsunami generation, which, although computed in the model, will not be detailed here.

Figure 1 shows the area of the Currituck slide complex, on the continental slope off of Chesapeake Bay. Grilli et al. (2015a) modeled tsunami generation for this slide using NHWAVE, representing it as a $V_s = 134$ km^3 rigid slump (i.e., within the range of the total volume estimated by Locat et al. (2009) for the failed area, 128–165 km^3), moving over a recreated unfailed bathymetry. Although the failure clearly occurred in two stages, as inferred from the two existing headwalls (Fig. 13a), the initial slump geometry was idealized as a single sediment mound with quasi-Gaussian cross sections and an elliptical footprint on the seafloor (Enet and Grilli 2007); maximum thickness was $T = 750$ m, downslope length $b = 30$ km, and width $w = 20$ km, with the ellipse centered at (-74.7E, 36.4N), in water depth $h \simeq 1800$ m (Fig. 13b). Assuming a bulk density $\rho_s = 1900\,\text{kg/m}^3$, the slump kinematics was specified as a bottom boundary condition in NHWAVE, based on the analytical law of motion developed by Grilli and Watts (2005), using the maximum velocity $U_{max} = 35$ m/s proposed by Locat et al. (2009) based on independent simulations with BING. With these parameters, the slump time of motion was found as $t_f = 11.9$ min and runout as $S_f = 15.8$ km (Fig. 13c).

Here, we repeat these simulations for the same recreated unfailed bathymetry and geometric representation of the SMF as in Grilli et al. (2015a) (Fig. 13b), but modeling its kinematics instead as a deforming Newtonian fluid-like layer of density $\rho_s = 1900$ kg/m^3. As shown in Figs. 10 and 11, changes in equivalent slide viscosity have a relatively smaller effect on slide kinematics and tsunami generation than changes in the bottom friction coefficient. Additionally, the analysis of field data for the Currituck slide complex (Prior et al. 1986; Locat et al. 2009) indicated that it had more likely failed as a high viscosity debris flow. Accordingly, and following Jiang and LeBlond (1992), we selected a fairly high equivalent slide viscosity $\mu_s = 500$ kg/(m s) corresponding to this type of rheology. We then varied the bottom friction coefficient n and observed its effect on the deforming slide kinematics; in the simulations, we used a horizontal grid with $\Delta x = \Delta y = 500$ m, covering the area of grid CT shown in Fig. 1 (see details in Table 1), and 5 σ-layers in the vertical direction. Note that this grid covers a fairly small area, extending more to the SE direction where the deforming slide is moving and tsunami generation occurs, which may not be sufficient to perform actual tsunami hazard assessment, but is sufficient at this stage for the purpose of comparing slide kinematics between rigid and deforming SMFs.

Figure 14 shows the slide center of mass motion S, velocity U and acceleration A computed during the NHWAVE simulations of the Currituck SMF, when specifying $n = 0.05$, 0.10, or 0.15, as compared to the kinematics of the equivalent rigid slump modeled by Grilli et al. (2015a). To properly compare tsunami generation for rigid and deforming SMFs, we selected $n = 0.1$, for which the slide motion and velocity during the majority of the failure (up to $t = 600$ s or 10 min) are closest to those of the rigid slump. This way, both the deforming and rigid SMF center of mass achieve approximately the same runout at the same time, while reaching a similar maximum velocity $U = 32$–34 m/s during motion. Based on these parameters, Fig. 15 shows snapshots of the modeled slide motion, from $t =$

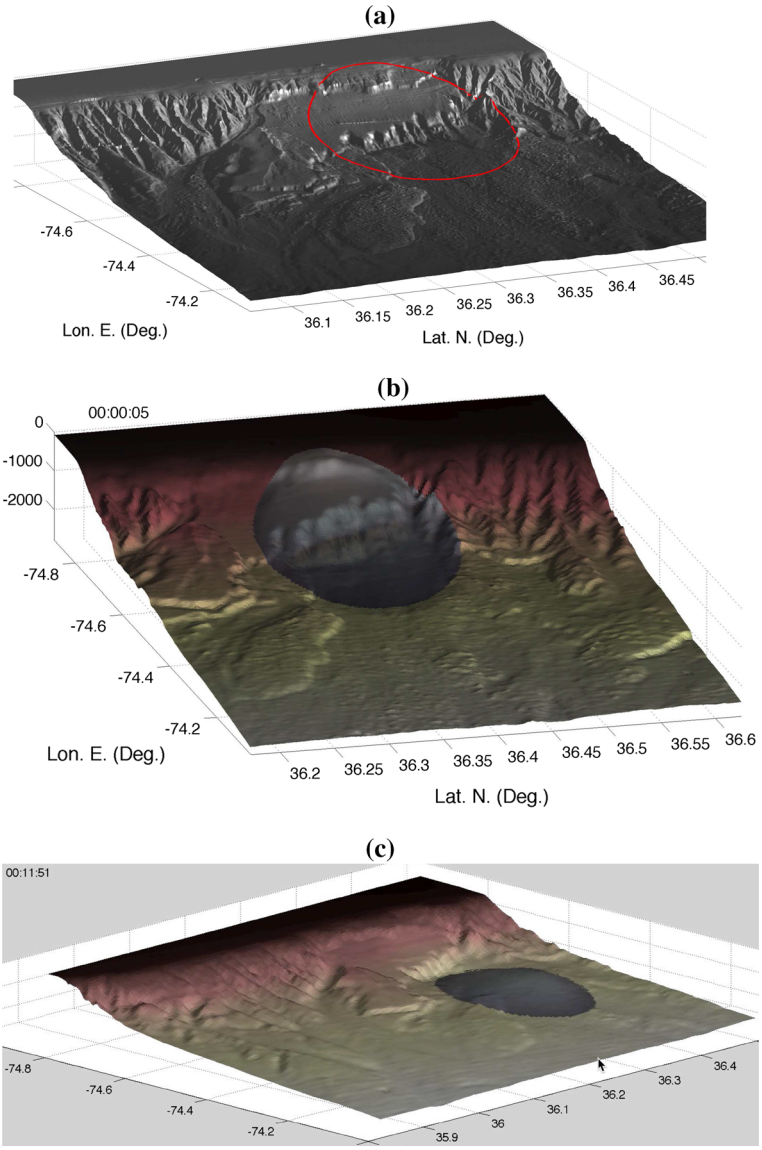

Fig. 13 Currituck slide complex (Fig. 1). **a** High-resolution bathymetry around the site in post-failed (current) conditions (the two headwalls identified by Locat et al. (2009) are clearly visible). **b** Zoom-in around initial slide location and assumed idealized geometry (V_s = 134 km^3; maximum thickness $T = 750$ m, downslope length $b = 30$ km, and width $w = 20$ km; density ρ_s =1900 kg/m^3), with the center of the pre-failed volume located at (−74.7 E, 36.4 N), in the unfailed recreated bathymetry. **c** Final location of rigid slump (Grilli et al. 2015a), at $t_f = 11.9$ min. Depth (<0) is marked in meters and time of 5 s marked in panel **b** corresponds to the first time step in NHWAVE

0–12 mins. We see that as the slide moves down the continental slope, it simultaneously vertically deforms and laterally spreads out, covering an increasingly large surface area on the seafloor. Comparing the snapshot in Fig. 15 at 12 min to the final slump motion in

Table 1 Parameters of Cartesian horizontal grids (Figs. 1, 16) used in NHWAVE (CT, G1) and FUNWAVE-TVD (G1, G2) models to compute tsunami generation by SMFs and propagation to the coast

Grid	SW Lat. (N°)	NE Lat. (N°)	SW Lon. (W°)	NE Lon. (W°)	Res. (m)	N_x	N_y
CT	35.430	36.559	74.900	72.7126	500	393	256
G1	37.401	40.993	74.464	69.838	1000	400	400
G2	40.003	40.967	74.437	72.245	154	1188	700

"Res." is grid resolution and N_x and N_y indicate the number of grid cells in each direction

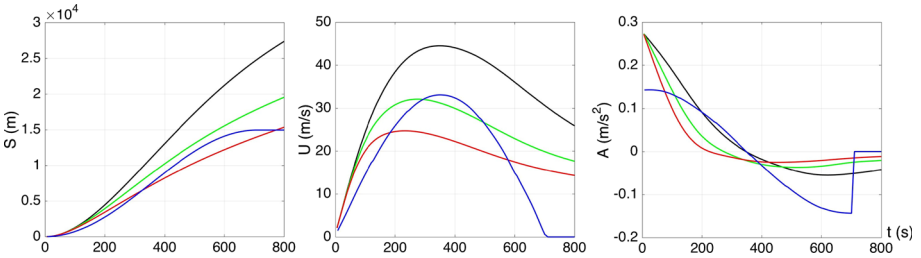

Fig. 14 Simulated kinematics of the Currituck SMF (Fig. 13). Time variation of center of mass motion S, velocity U, and acceleration A, for a deforming fluid-like slide, with $\mu_s = 500$ kg/(m s) and a Manning friction coefficient $n = 0.05$ (*black*), 0.10 (*green*), and 0.15 (*red*), as compared to Grilli et al.'s (2015a) rigid slump kinematics (*blue*)

Fig. 13c, we see that, by contrast, the slump is just performing a pendulum-like rigid motion, while keeping its shape and footprint on the seafloor constant.

4.2 Hudson River canyon SMF

We simulate tsunami generation and propagation to the coast by a Currituck SMF proxy located in Area 1 of Fig. 1, in the Hudson River Canyon (Fig. 16), and evaluate effects of slide rheology on coastal tsunami hazard in terms of maximum surface elevation near the coast (at the 5-m isobath). The SMF proxy has the same volume and geometry as that assumed for the Currituck slide: $V_s = 134$ km^3 and a quasi-Gaussian initial geometry of thickness $T = 750$ m and elliptical footprint on the seafloor, of downslope length $b = 30$ km and width $w = 20$ km (see footprint in Fig. 16). Because this is a hypothetical SMF occurring on an existing slope, its failure is assumed to occur below seafloor (by contrast with the actual Currituck paleoslide whose initial geometry was recreated over the current seafloor). We simulate the SMF motion and corresponding tsunami generation with NHWAVE, assuming that it behaves either as a rigid slump (as in Grilli et al. 2015a) or as a deforming fluid-like slide. Once tsunami generation is completed in NHWAVE, simulations are initialized and continued with FUNWAVE-TVD.

In the rigid slump simulation, the SMF has a pendulum-like motion in the assumed azimuthal direction $\theta = 136°$. (from north), and its geometry and kinematics, similar to that shown in Fig. 14 (computed as detailed in Grilli et al. 2015a), are specified as a bottom boundary condition in NHWAVE. In this simulation, as in Grilli et al. (2015a), bottom friction between water and the rigid slide is neglected, which is acceptable considering the large water depth. In the deforming slide simulations, tsunami generation is computed with

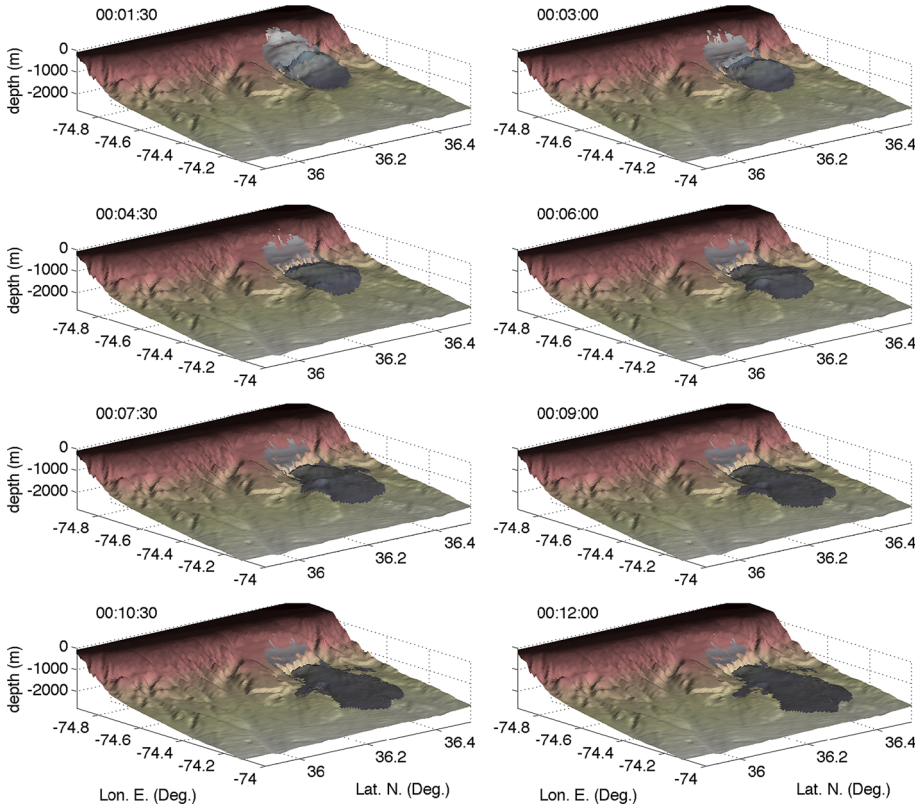

Fig. 15 Currituck slide complex (Fig. 13). Snapshots of deforming slide motion modeled using NHWAVE, with a dense fluid layer underneath, assuming $\mu_s = 500$ kg/(m s) and a Manning friction coefficient $n = 0.10$. Time of snapshots is marked in min:s

the two-layer NHWAVE model, in which the dense fluid bottom layer has parameters similar to those calibrated above for the historical Currituck slide case, i.e., , $\rho_s = 1900$ kg/m^3, $\mu_s = 500$ kg/(m s), and $n = 0.05$, 0.1, or 0.15 for the slide–substrate bottom friction. With these parameters and $n = 0.1$, the above simulations of the historical Currituck SMF showed that the deforming slide nearly reached the same runout S_f as the rigid slump at time t_f (see details above and Fig. 14). Although the bottom topography is different in Area 1, we find that for these parameters the law of motion of the Currituck SMF proxy near the Hudson River Canyon is very close to that derived for the historical Currituck slide, whether modeled as a rigid slump or a deforming slide, both shown in Fig. 14; hence, the Hudson Canyon SMF kinematics is not replotted here.

Figure 16a shows the boundary of two nested grids used in simulations (see details in Table 1). Tsunami generation was first computed with NHWAVE in the 1000-m-resolution Cartesian grid G1, with 5 σ-layers in the vertical direction, up to $t = 20$ min, when the deforming slide motion becomes negligible. At time $t > t_f = 11.9$ min, when the rigid SMF stops moving, we find that the deforming slide, although still moving and spreading out, is no longer significantly tsunamigenic, due to both its gradual thinning out and the large depth (see Figs. 17b, 18b, discussed later). Hence, following Grilli et al. (2015a),

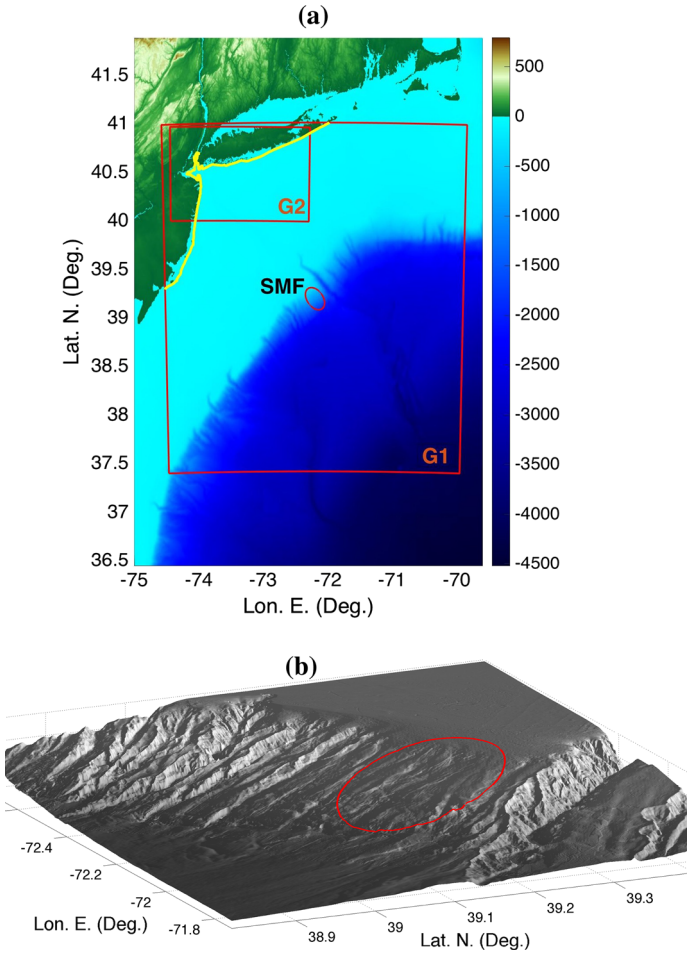

Fig. 16 Simulations of tsunami generation by a Currituck SMF proxy located in the Hudson River Canyon (area 1 in Fig. 1). **a** Boundary (*red lines*) of nested Cartesian grids used in simulations: G1 (1000 m resolution) and G2 (154 m resolution) (see details in Table 1). Tsunami generation is performed in grid G1 using NHWAVE with 5 σ-layers in the vertical direction, and results are used as initial condition in FUNWAVE-TVD, also for grid G1. The *thick yellow line marks* the 5-m-depth isobath along which tsunami elevation is computed in Fig. 19. **b** Zoom-in on SMF location, with the Hudson River canyon visible to the east of it. *Color scale* in **a** is bathymetry (<0) and topography (>0) in meters. *Red ellipses mark* the SMF footprint

computations of tsunami propagation and coastal impact, for both rigid and deforming SFMs, were pursued with FUNWAVE-TVD for $t > 13.3$ min (800 s), by initializing it with the surface elevations (Fig. 17c, d) and corresponding horizontal velocities interpolated at the relevant depth ($0.531h$; Shi et al. 2012), computed at this time with NHWAVE. However, while this was straightforward for the rigid slump, which was no longer moving, for the still moving deforming slide, initializing FUNWAVE-TVD at this time caused the appearance of a large spurious rebound wave, likely due to inconsistencies in bottom boundary conditions. Hence, simulations with NHWAVE were pursued until $t =$ 20 min (1200 s) before initializing FUNWAVE-TVD, which prevented the appearance of

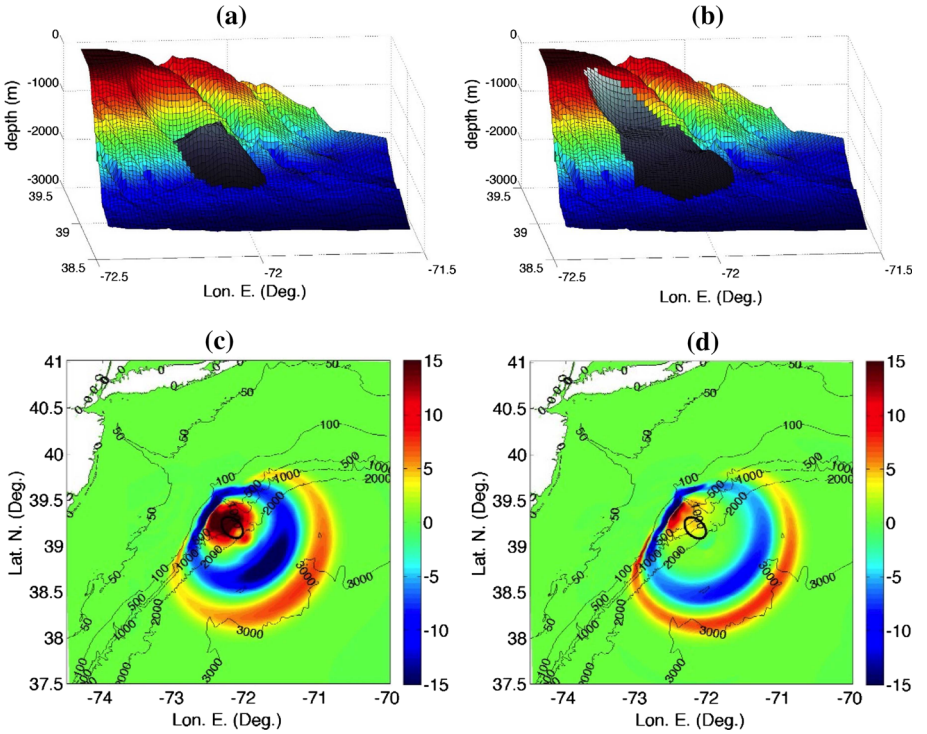

Fig. 17 NHWAVE simulations in grid G1 of tsunami generation by a Currituck SMF proxy sited in Area 1 (Fig. 1) in the Hudson River Canyon (Fig. 16), modeled as a: **a**, **c** rigid slump (Grilli et al. 2015a); **b**, **d** deforming slide represented by a dense fluid layer (with $\mu_s = 500$ kg/(m s) and $n = 0.1$), of same initial geometry, location, volume, density $\rho_s = 1900$ kg/m^3, and runout at the time the slump stops moving ($t_f = 11.9$ min). Panels **a**, **b** show in gray the SMF locations after 13.3 min (to the West of the Hudson River canyon), and panels **c**, **d** show the surface waves generated after 13.3 min (800 s; the *black ellipses mark* the initial footprint of the SMFs)

the spurious wave in the deforming slide case; for consistency, initialization was done at the same time for the rigid slump case as well. In both cases, for $t > 20$ min, FUNWAVE-TVD is first run in grid G1 and then by one-way coupling in the 154-m-resolution grid G2; in these simulations, a Manning coefficient $n = 0.025$ (i.e., the value for coarse sand) was used to define bottom friction.

Figure 17 shows results of NHWAVE simulations for slide motion and wave generation at time $t = 13.3$ min (800 s), for both the rigid slump and the deforming slide (i.e., shortly after the slump stops moving). At this time, whereas the rigid slump has moved in the specified downslope direction (transect in Fig. 18a) while preserving its shape, the deforming slide has flown asymmetrically, following the steepest slope on the seafloor, while spreading in all directions (Fig. 17a, b). Figure 18b shows a downslope transect through the time-dependent bathymetry of both the rigid slump and the deforming slide; here, we see as expected that both SMFs achieve approximately the same runout when the slump stops moving (at $t = 714$ s). However, as a result of lateral spreading, the deforming slide thickness over the seafloor gradually reduces along the transect. Also note that, at $t =$ 300 s, both SMFs approximately have the same cross section along their axis, indicating that lateral spreading of the deforming slide is not very significant at small time, likely as a

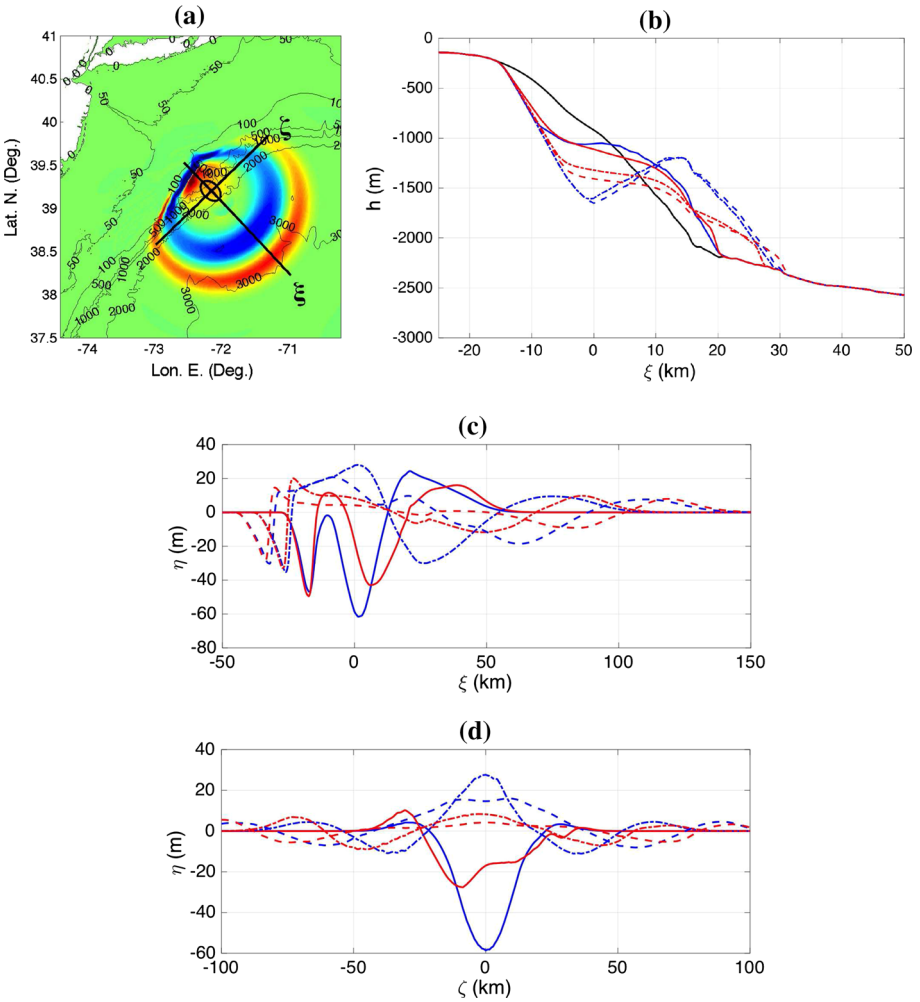

Fig. 18 Case of Fig. 16. Transects marked in panel **a** (centered on SMF's initial location): **b**, **c** downslope (ξ; azimuth $\theta = 136°$ from North) and **d** cross-slope (ζ). Transects show: **b** bottom topography and SMFs and **c**, **d** tsunami waves generated, by a rigid slump (*blue*) and a deforming slide (*red*), simulated with NHWAVE. Times in panels **b**–**d** are t = 300 (*solid*), 600 (*chained*), and 800 (*dashed*) s

result of the high slide viscosity. Despite the difference in kinematics and geometry, the patterns of generated tsunami waves shown in Fig. 17c, d at t = 13.3 min are similar for both SMFs. As a result of variations in thickness over the seafloor, there is a marked asymmetry in wave generation for the deforming slide, with larger waves being generated on its western side; this is further discussed below. Overall, results show that onshore moving waves have lower elevations in the deforming slide case.

Differences in generated waves for both SMFs are more apparent in the transects of Fig. 18c, d through free surface elevations computed with NHWAVE, downslope (Fig. 18c; ξ direction, $\theta = 136°$ from north) and cross-slope (Fig. 18d; ζ direction), at time t = 300, 600, and 800 s (13.3 min). At t = 300 s, in both cases, the free surface is essentially a deep two-pronged depression with a large elevation wave that has propagated offshore.

The depression in the free surface, which is due to the draw down caused by the large volume of sediment moving downslope, has a deeper offshore trough for the rigid slump (60 m deep) than for the deforming slide (about 28 m deep), and a second onshore through of closely identical shape and nearly 50 m deep in both cases. For both SMFs, at $t = 300$ s, a rebound wave has already formed in the middle of the depression. Figure 18c shows that, at $t = 600$ and 800 s, this rebound wave propagates onshore as the first elevation wave of both SMF tsunami wave trains, preceded by a depression wave resulting from the initial onshore trough caused by the SMF drawdown. At these times, for both SMFs, the offshore elevation wave and trough propagate faster offshore (due to the increase in phase velocity over the deep ocean), while decreasing in elevation as a result of the 2D horizontal energy spreading (Fig. 17c, d; also visible in the cross-slope transects of Fig. 18d). The cross-slope transects (Fig. 18d) show that while waves generated by the rigid slump are fairly symmetrical with respect to the SMF axis of motion ($\zeta = 0$), those generated by the deforming slide are larger on its western side ($\zeta < 0$) than on its eastern side, and the maximum initial free surface depression shown at $t = 300$ s is also shifted westward, whereas it is on the SMF axis for the rigid slump. As discussed above, this results from the asymmetry of the deforming slide thickness on the seafloor.

For $t > 20$ min, for both rigid and deforming SMFs, simulations are initialized with NHWAVE's results and pursued with FUNWAVE-TVD in grid G1, up to 3 h 8' of tsunami propagation (note that sponge layers are specified along the grid boundary), and time series of surface elevations are computed along the boundary of the 154-m-resolution nested grid G2, to be used in the one-way coupling methodology. Simulations are then restarted from $t = 0$ in grid G2, and forced with the time series used as boundary conditions. Note that, similar to Grilli et al. (2015a), for sake of computational efficiency, before initializing simulations in FUNWAVE-TVD the offshore propagating waves are filtered out, allowing to use a smaller domain in both models and narrower sponge layers in FUNWAVE-TVD, that do not significantly interfere with the coastline of interest. This filtering was done to the right of a diagonal line, which is visible in Fig. 19a, b, and it was verified that this did not affect results in the main area of interest in grid G2 (whose limits are shown in both figures).

Figure 19a, b shows envelopes of maximum surface elevations η_{max} computed in grids G1 and G2 during simulations with FUNWAVE-TVD, for rigid and deforming (with $n = 0.025$) SMFs, respectively. While patterns and directionality of the maximum envelopes are similar, as expected, there is a marked westward increase in wave generation for the deforming slide case. Overall, the maximum height of waves generated by the rigid slump is larger (over 25 m near the source; see also Fig. 18c, d) than for the deforming slide (up to 12 m near the source). As waves propagate onshore over the wide shallow shelf, in both cases, surface elevations significantly decrease and are similarly modulated alongshore, as a result of bottom friction dissipation over the wide shallow shelf and bathymetric control on wave focusing/defocusing, respectively (Tehranirad et al. 2015).

Coastal tsunami hazard is quantified in Fig. 19c, in terms of envelopes of maximum surface elevations computed along the 5-m isobath marked by a yellow line in Figs. 16 and 19a, b; this is similar to Grilli et al. (2015a) who compared maximum tsunami elevations simulated for various sources at a 5-m isobath along the USEC. In Fig. 19c, the alongshore variation of maximum wave elevation η_{max} computed in grid G2 for both SMFs is plotted as a function of the curvilinear distance s along the isobath. The middle section of this isobath (centered around 225 km) is within the Hudson River Estuary complex where, due to bathymetric defocusing, tsunami elevations are significantly lower than those impacting the coasts of Long Island (<210 km) and New Jersey (>260 km) (see Shelby et al. 2016 for

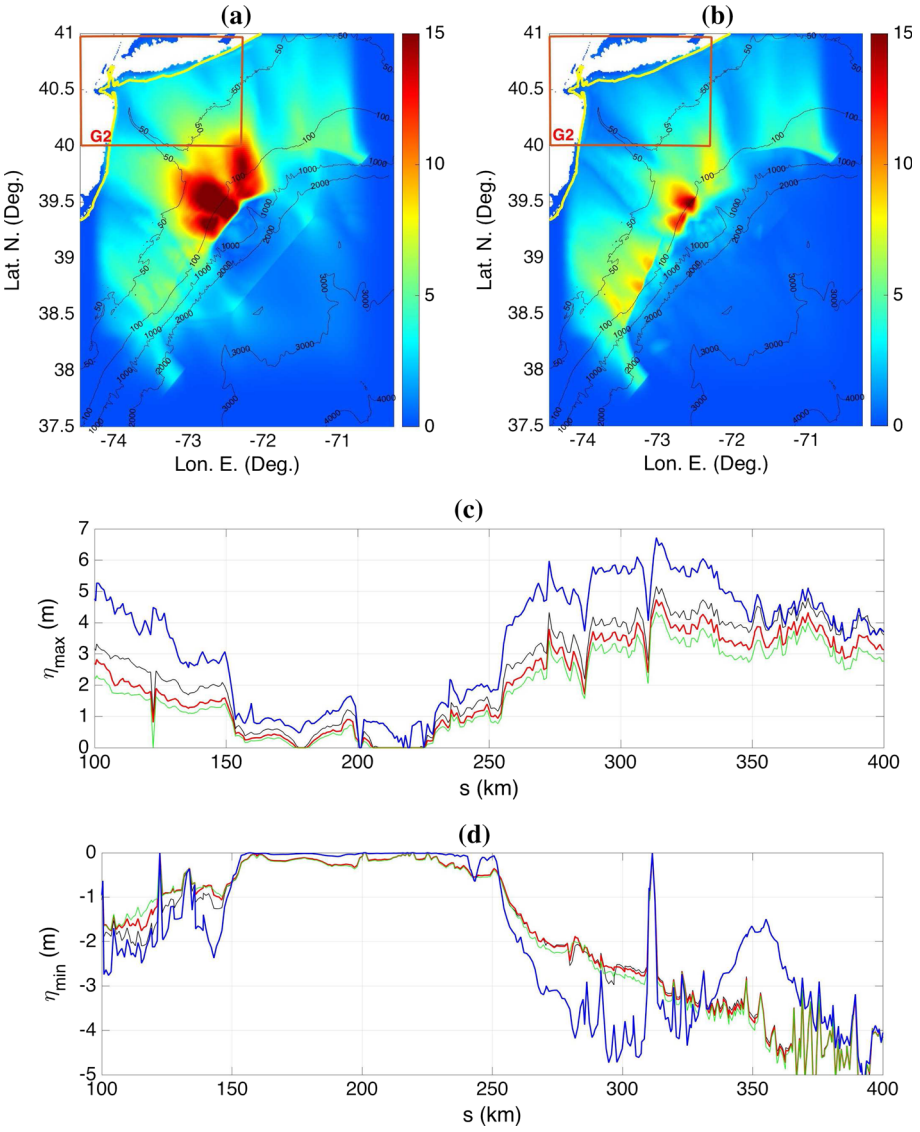

Fig. 19 Case of Figs. 16, 17, and 18. Envelopes of maximum surface elevation η_{max} (color scale in meters) computed with FUNWAVE-TVD in grids G1 and G2 up to 3 h 8 min (initialized at t = 20 min with NHWAVE's results; n = 0.025) during propagation of SMF tsunamis generated by: **a** a rigid slump, and **b** a deforming slide (with n = 0.10 in NHWAVE) (bathymetric contours are shown in meters). Based on grid G2 results, envelopes of: **c** maximum η_{max} and **d** minimum η_{min} surface elevations computed along the 5-m isobath (*yellow line* marked in (**a**, **b**)), for tsunamis generated by a rigid slump (*thick blue*), and three different deforming slides with $n = 0.05n = 0.05$ (*black*), n = 0.10 (*thick red*), and n = 0.15 (*green*), for the slide–substrate bottom friction; the curvilinear distance s along the 5-m contour is computed from its southern end; the region of lower maximum surface elevations (210–260 km) corresponds to the Hudson River Estuary complex, with the New Jersey shore to the south (*left*), and Long Island shore to the north (*right*)

details). Consistent with the maximum envelopes of Fig. 19a, b, maximum surface elevations near the coast caused by the rigid slump are larger at most locations, by up to a factor of 2, as compared to waves generated by the reference deforming slide case (with $n = 0.10$). As pointed out by Tehranirad et al. (2015), waves generated in both cases, although of different height, have similar patterns of alongshore variation, due to the bathymetric control on long wave focusing/defocusing. For comparison, the figure also shows maximum surface elevations caused by deforming slides with a reduced or a larger slide–substrate friction (i.e., $n = 0.05$ or 0.15), and expectedly these change as the inverse of n. Reducing friction in the deforming slide, however, is not sufficient to cause surface elevations that are larger than those of the rigid slump, except slightly in a very small area to the right of the figure.

Finally, some critical coastal infrastructures, such as power plants, which have cold water intakes, are also severely impacted by low water conditions, that occur during the initial SMF tsunami impact in the form of a large leading depression wave. Hence, in Fig. 19d, we similarly plotted the envelope of minimum surface elevations η_{min} computed along the 5-m isobath for all SMF cases considered in Fig. 19c. Consistent with the larger initial depression wave it generates, we see that the rigid slump also causes a larger drawdown at the coast at most locations than the deforming slide cases, except to the north of the isobath (for $x > 330$ km), likely due to site-specific bathymetric effects.

5 Discussion and conclusions

In this work, we first validated two models simulating tsunami generation by deforming submarine mass failures (SMFs), against laboratory experiments conducted at IRPHE in a small precision wave tank. One case was used, from a large set of highly repeatable laboratory experiments performed for SMFs made of glass beads moving down a steep slope. Both validated models are two-layer models in which fluid motion is simulated with the 3D (σ-layer) non-hydrostatic model NHWAVE and the SMF layer is depth-integrated and represented by either a dense Newtonian fluid (Kirby et al. 2016) or a granular flow (Ma et al. 2015). The latter model is currently limited to a plane slope and does not include dilatancy effects in the granular medium. Both models currently neglect vertical accelerations and hence should be more accurate for moderate to small slopes. Additional sensitivity analyses were performed for the dense fluid model, including assessing model convergence regarding both horizontal and vertical grid resolution, and sensitivity of slide motion and generated surface elevations to slide parameters: specifically, result sensitivity to slide viscosity (i.e., internal energy dissipation), bottom friction, and initial submergence.

Overall, once calibrated, results of both models were found in good agreement with time series of surface elevations measured at 4 gages. The agreement at gage WG1 was slightly better with the dense flow model, but that at gages WG2–WG4 was slightly better with the granular flow model. Both models provided a similarly good simulation of both the salient features, and geometry and kinematics of the moving slide material. The dense fluid slide model, which at present is the only one that can be applied to an arbitrary bottom bathymetry, was then used to simulate the historic Currituck SMF motion, in order to determine relevant viscous slide parameters to simulate SMF tsunamis on the USEC. This historical SMF and the generated tsunami were previously modeled by Grilli et al. (2015a) as a rigid slump. Here, slide parameters were first adjusted based on sediment properties, as

well as to match the earlier values of the Currituck SMF runout and maximum velocity, when simulated as a rigid slump. Having determined that slide behavior is more sensitive to bottom friction than viscosity at this scale, particularly on the mild continental slope, assuming for this moderately deforming slide a large viscosity $\mu_s = 500$ kg/(m s), 3 values of Manning's n coefficient (n = 0.05, 0.10, and 0.15) were selected to cover a realistic range of possible deforming slide rheologies.

The same parameters were finally applied to simulate tsunami generation from a possible SMF sited near the Hudson River Canyon. As for Currituck, this SMF had also been simulated by Grilli et al. (2015a) as a rigid slump, as this was expected to provide a conservative (i.e., worst case scenario) estimate of tsunami generation and coastal impact, adequate for NTHMP tsunami hazard mapping. Simulations were performed as before for 3 deforming slides and the rigid slump, and results compared; all SMFs had the same initial volume, location, and geometry. The SMFs' center of mass motion, velocity, and acceleration were compared and it was verified that the deforming slide with n = 0.1 nearly achieved the same runout as the rigid slump, at the time the latter stopped moving. While initial acceleration was larger for the deforming slides, both velocity and accelerations stayed larger for a longer time for the rigid slump; this, combined with the reducing thickness of the deforming slide during motion led to a smaller tsunami generation in all cases of deforming slides than for the rigid slump.

Tsunami propagation was computed for the 4 generated tsunamis using the 2D long wave model FUNWAVE-TVD in two levels of nested grids, and maximum surface elevations were computed along a 5-m-depth contour off of the coast of New Jersey and New York. From very large initial surface elevations (up to 25 m for the rigid slump), nearshore tsunami elevations were found to be significantly smaller in all cases (up to 6.5 m), due to both directional energy spreading and bottom friction over the wide shelf. At most locations, nearshore tsunami surface elevations caused by the rigid slump were found to be significantly larger (up to a factor of 2) than those caused by the 3 deforming slide cases; for those, surface elevation slightly increased when n decreased. Nearshore minimum surface elevations (tsunami drawdown) were similarly computed, and it was found, again, that the rigid slump caused the largest drawdown in most cases, except along a stretch of the coast of Long Island, likely due to site specific focusing bathymetric effects.

In view of these results (see Fig. 19), we conclude that, as expected from earlier work (e.g., Watts and Grilli 2003; Grilli and Watts 2005), the rigid slump provides a conservative estimate of SMF tsunami coastal hazard, in terms of maximum inundation/run-up at the coast and, in most locations, of maximum drawdown. By contrast, using a more realistic rheology with some level of SMF deformation, in general, will reduce tsunami impact at the coast, whether maximum inundation or drawdown are considered. This validates as conservative the tsunami hazard assessment and inundation mapping performed to date along the USEC, as part of NTHMP, on the basis of Currituck SMF proxies simulated as rigid slump (Grilli et al. 2015a).

While the dense fluid NHWAVE model is adequate for simulating the SMFs that should most likely occur off of the USEC, in the form of debris flows with a significant mud content, the two-layer granular flow NHWAVE model features more complete and realistic physics and thus has the potential of better modeling SMF tsunami generation in a greater variety of context and rheology. This, however, will require this model to be extended to arbitrary bottom topography; as indicated, this extension is in progress. Additionally, it is planned in future work to improve the granular layer depth-integrated governing equations to properly include effects of vertical accelerations, which may be important for steeper slopes, and dilatancy. The latter was for instance included in the two-phase model recently

proposed by Bouchut et al. (2016), who indicate that when dilation occurs the fluid is sucked into the granular material, the pore pressure decreases and the friction force on the granular phase increases. In the case of contraction (the opposite of dilation), the fluid is expelled from the mixture, the pore pressure increases and the friction force decreases. Including dilatancy will thus allow simulating both volumetric and bed dissipation effects that realistically vary with slide shape and kinematics. The authors believe that this approach has greater potential than dynamically and empirically varying the bed friction coefficient value as slide material is spreading and thinning out, as proposed, e.g., by Yavari-Ramshe and Ataie-Ashtiani (2015).

Many of the issues discussed above relative to relevant deforming SMF rheology and modeling are complex and the object of active research. In this respect, a landslide tsunami model benchmarking workshop, organized by some of the authors, will be held in Galveston, TX (http://nws.weather.gov/nthmp/2017MMSLandslide/index.html), in January 2017, where all the NTHMP investigators and many international landslide tsunami experts will meet to discuss the modeling and physics of SMF tsunamis. The glass bead experiments reported in this paper will be used as the workshops, Benchmark 4 (out of 7 benchmarks).

Acknowledgements SG, JK, and GM acknowledge support from grant CMMI-15-35568 of the United States (US) National Science Foundation (NSF), Engineering for Natural Hazard program; SG, MS, JK, and FS from grant NA-15-NWS-4670029 of the National Tsunami Hazard Mitigation Program (NTHMP) from the US Department of Commerce/National Oceanic at Atmospheric Administration (NOAA). DN's research in this publication was sponsored by the State of Alaska and also by the University of Alaska Fairbanks Cooperative Institute for Alaska Research, with funds from NOAA under cooperative agreement NA-08-OAR-4320751 with the University of Alaska. This does not constitute an endorsement by NOAA.

References

Abadie S, Morichon D, Grilli ST, Glockner S (2008) VOF/Navier-Stokes numerical modeling of surface waves generated by subaerial landslides. La Houille Blanche 1:21–26. doi:10.1051/lhb:2008001

Abadie S, Morichon D, Grilli ST, Glockner S (2010) Numerical simulation of waves generated by landslides using a multiple-fluid Navier–Stokes model. Coast Eng 57:779–794. doi:10.1016/j.coastaleng.2010.03.003

Abadie S, Harris JC, Grilli ST, Fabre R (2012) Numerical modeling of tsunami waves generated by the flank collapse of the Cumbre Vieja Volcano (La Palma, Canary Islands): tsunami source and near field effects. J Geophys Res 117:C05030. doi:10.1029/2011JC007646

Assier-Rzadkiewicz S, Mariotti C, Heinrich P (1997) Numerical simulation of submarine landslides and their hydraulic effects. J Waterw Port Coast Ocean Eng 123:149–157

Ataie-Ashtiani B, Najafi-Jilani A (2006) Prediction of submerged landslide generated waves in dam reservoirs: an applied approach. Dam Eng 17(3):135–155

Ataie-Ashtiani B, Najafi-Jilani A (2007) A higher-order Boussinesq-type model with moving bottom boundary: applications to submarine landslide tsunami waves. Int J Numer Meth Fluid 53(6):1019–1048. doi:10.1002/fld.1354

Ataie-Ashtiani B, Nik-khah A (2008) Impulsive waves caused by subaerial landslides. Environ Fluid Mech 8(3):263–280. doi:10.1007/s10652-008-9074-7

Ataie-Ashtiani B, Najafi-Jilani A (2008) Laboratory investigations on impulsive waves caused by underwater landslide. Coast Eng 55(12):989–1004. doi:10.1016/j.coastaleng.2008.03.003

Ataie-Ashtiani B, Shobeyri G (2008) Numerical simulation of landslide impulsive waves by incompressible smoothed particle hydrodynamics. Intl J Num Meth Fluids 56(2):209–232

Barkan R, ten Brick US, Lin J (2009) Far field tsunami simulations of the 1755 Lisbon earthquake: implication for tsunami hazard to the US East Coast and the Caribbean. Mar Geol 264:109–122

Bouchut F, Fernández-Nieto ED, Mangeney A, Narbona-Reina G (2016) A two-phase two-layer model for fluidized granular flows with dilatancy effects. J Fluid Mech 801:166–221. doi:10.1017/jfm.2016.417

Chaytor J, ten Brink US, Solow J, Andrews BD (2009) Size distribution of submarine landslides along the U.S. Atlantic Margin. Mar Geol 264:16–27

Day SJ, Watts P, Grilli ST, Kirby JT (2005) Mechanical models of the 1975 Kalapana, Hawaii earthquake and tsunami. Mar Geol 215:59–92. doi:10.1016/j.margeo.2004.11.008

Day SJ, Llanes P, Silver E, Hoffmann G, Ward SN, Driscoll N (2015) Submarine landslide deposits of the historical lateral collapse of Ritter Island, Papua New Guinea. Mar Petrol Geol 67:419–438

De Blasio FV, Engvik L, Harbitz CB, Elverhøi A (2004) Hydroplaning and submarine debris flows. J Geophys Res 109. doi:10.1029/2002JC001714

Eilers H (1941) Die Viskosität von Emulsionen hochviskoser Stoffe als Funktion der Konzentration. Kolloid-Zeitschrift 97(3):313–321

Enet F, Grilli ST, Watts P (2003) Laboratory experiments for tsunamis generated by underwater landslides: comparison with numerical modeling. In Proceedings of 13th offshore and polar engineering conference (ISOPE03, Honolulu, USA, May 2003), pp 372–379

Enet F, Grilli ST (2007) Experimental study of tsunami generation by three-dimensional Rigid underwater landslides. J Waterw Port Coast Ocean Eng 133(6):442–454

Fernández-Nieto ED, Bouchut F, Bresch D, Castro Diaz MJ, Mangeney A (2008) A new Savage-Hutter type model for submarine avalanches and generated tsunami. J Comp Phys 227:7720–7754

Fine IV, Rabinovich AB, Bornhold BD, Thomson R, Kulikov EA (2005) The Grand Banks landslide-generated tsunami of November 18, 1929: preliminary analysis and numerical modeling. Mar Geol 215:45–57

Fine IV, Rabinovich AB, Kulikov EA et al (1998) Numerical modelling of landslide generated tsunamis with application to the Skagway Harbor tsunami of November 3, 1994. Proceedings of international conference on Tsunamis, Paris, pp 211–223

Fritz HM, Hager WH, Minor H-E (2001) Lituya bay case: rock slide impact and wave runup. Sci Tsunami Hazards 19:3–22

Fritz HM, Hager WH, Minor H-E (2004) Nearfield characteristics of landslide generated impulse waves. J Waterw Port Coast Ocean Eng 130:287–302

Fuhrman DR, Madsen PA (2009) Tsunami generation, propagation, and run-up with a high-order Boussinesq model. Coast Eng 56:747–758. doi:10.1016/j.coastaleng.2009.02.004

Fujii Y, Satake K, Sakai S, Shinohara M, Kanazawa T (2011) Tsunami source of the 2011 off the Pacific coast of Tohoku, Japan earthquake. Earth Planets Space 63:815–820

Frankel NA, Acrivos A (1967) On the viscosity of a concentrated suspension of solid spheres. Chem Eng Sci 22(847–853):1016. doi:10.1016/0009-2509(67)80149-0

Fryer GJ, Watts Ph, Pratson LF (2004) Source of the great tsunami of 1 April 1946: a landslide in the upper Aleutian forearc. Mar Geol 203:201–218

Geist E, Lynett P, Chaytor J (2009) Hydrodynamic modeling of tsunamis from the Currituck landslide. Mar Geol 264:41–52. doi:10.1016/j.margeo.2008.09.005

Glicken H (1996) Rockslide-Debris Avalanche of May 18, 1980, Mount St. Helens Volcano, Washington. USGS Open-file Report 96-677, US Geological Survey, Reston

Glimsdal S, Pedersen GK, Harbitz CB, Løvholt F (2013) Dispersion of tsunamis: does it really matter? Nat Hazards Earth Syst Sci 13:1507–1526. doi:10.5194/nhess-13-1507-2013

Grilli ST, Ioualalen M, Asavanant J, Shi F, Kirby JT, Watts P (2007) Source constraints and model simulation of the December 26, 2004 Indian Ocean tsunami. J Waterw Port Coast Ocean Eng 33:414–428

Grilli ST, Dias, F Guyenne, P Fochesato C and F Enet (2010a) Progress In fully nonlinear potential flow modeling of 3D extreme ocean waves. Chapter 3 in Advances in Numerical Simulation of Nonlinear Water Waves (ISBN: 978-981-283-649-6, edited by Q.W. Ma) (Vol. 11 in Series in Advances in Coastal and Ocean Engineering). World Scientific Publishing Co. Pte. Ltd., pp. 75–128

Grilli ST, Dubosq S, Pophet N, Pérignon Y, Kirby JT, Shi F (2010) Numerical simulation and first-order hazard analysis of large co-seismic tsunamis generated in the Puerto Rico trench: near-field impact on the North shore of Puerto Rico and far-field impact on the US East Coast. Nat Hazards Earth Syst Sci 10:2109–2125. doi:10.5194/nhess-2109-2010

Grilli ST, Harris JC, Tajalibakhsh T, Masterlark TL, Kyriakopoulos C, Kirby JT, Shi F (2013) Numerical simulation of the 2011 Tohoku tsunami based on a new transient FEM co-seismic source: Comparison to far- and near-field observations. Pure Appl Geophys 170:1333–1359. doi:10.1007/s00024-012-0528-y

Grilli ST, O'Reilly C, Harris JC, Tajalli-Bakhsh T, Tehranirad B, Banihashemi S, Kirby JT, Baxter CDP, Eggeling T, Ma G, Shi F (2015a) Modeling of SMF tsunami hazard along the upper US East Coast: detailed impact around Ocean City. MD Nat Hazards 76(2):705–746. doi:10.1007/s11069-014-1522-8

Grilli ST, Grilli AR, Tehranirad B and JT Kirby (2015b) Modeling tsunami sources and their propagation in the Atlantic Ocean for coastal tsunami hazard assessment and inundation mapping along the US East Coast. In Proceedings of 2015 COPRI solutions to coastal disasters conference, (Boston, USA. September 9–11, 2015), American Soc Civil Eng (in press)

Grilli ST, Taylor O-DS, Baxter CDP, Maretzki S (2009) Probabilistic approach for determining submarine landslide tsunami hazard along the upper East Coast of the United States. Mar Geol 264(1–2):74–97

Grilli ST, Vogelmann S, Watts P (2002) Development of a 3D numerical wave tank for modeling tsunami generation by underwater landslides. Eng Anal Bound Elem 26(4):301–313

Grilli ST, Watts P (1999) Modeling of waves generated by a moving submerged body. Applications to underwater landslides. Eng Anal Bound Elem 23:645–656

Grilli ST, Watts P (2005) Tsunami generation by submarine mass failure, I: modeling, experimental validation, and sensitivity analyses. J Waterw Port Coast Ocean Eng 131(6):283–297

Harbitz CB (1992) Model simulations of tsunamis generated by the Storegga slides. Mar Geol 105:1–21

Harbitz C, Pedersen G, Gjevik B (1993) Numerical simulations of large water waves due to landslides. J Hydraul Eng 119:1325–1342

Heinrich P (1992) Nonlinear water waves generated by submarine and aerial landslides. J Waterw Port Coast Ocean Eng 118:249–266

Heller V, Hager WH (2010) Impulse product parameter in landslide generated impulse waves. J Waterw Port Coastal Ocean Eng. 136:145155

Horrillo J, Wood A, Kim GB, Parambath A (2013) A simplified 3-D Navier–Stokes numerical model for landslide-tsunami: application to the Gulf of Mexico. J Geophys Res 118:6934–6950. doi:10.1002/2012JC008689

Hungr O, Evans SG, Bovis MJ, Hutchinson JF (2001) A review of the classification of landslides of the flow type. Environ Eng Geosci 7:221–238

Imran J, Parker G, Locat J, Lee H (2001) 1D numerical model of muddy subaqueous and subaerial debris flow. J Hyd Eng ASCE 127(11):959–968

Ioualalen M, Asavanant J, Kaewbanjak N, Grilli ST, Kirby JT, Watts P (2007) Modeling the 26th December 2004 Indian Ocean tsunami: case study of impact in Thailand. J Geophys Res 112:C07024. doi:10.1029/2006JC003850

Iverson RM, Denlinger RP (2001) Flow of variably fluidized granular masses across three-dimensional terrain 1. Coulomb mixture theory. J Geophys Res 106:537–552

Jiang L, LeBlond PH (1992) The coupling of a submarine slide and the surface waves which it generates. J Geophys Res 97(C8):12731–12744

Jiang L, Leblond PH (1993) Numerical modeling of an underwater Bingham plastic mudslide and the waves which it generates. J Geophys Res 98:10303–310317

Kirby JT, Shi F, Tehranirad B, Harris JC, Grilli ST (2013) Dispersive tsunami waves in the ocean: model equations and sensitivity to dispersion and Coriolis effects. Ocean Modell 62:39–55. doi:10.1016/j.ocemod.2012.11.009

Kirby JT, Shi F, Nicolsky D, Misra S (2016) The 27 April 1975 Kitimat, British Columbia submarine landslide tsunami: a comparison of modeling approaches. Landslides 2016: doi:10.1007/s10346-016-0682-x (published online Feb. 26)

Liu PL-F, Wu T-R, Raichlen F, Synolakis CE, Borrero JC (2005) Runup and rundown generated by three-dimensional masses. J Fluid Mech 536:107–144

Locat J, Lee H, ten Brink US, Twichell D, Geist E, Sansoucy M (2009) Geomorphology, stability and mobility of the Currituck slide. Mar Geol 264:28–40

Løvholt F, Pedersen G, Gisler G (2008) Oceanic propagation of a potential tsunami from the La Palma Island. J Geophys Res 113:C09026

Lynett P, Liu PL-F (2002) A numerical study of submarine landslide generated waves and runup. Proc R Soc Lond A458:2885–2910

Lynett P, Liu PL-F (2005) A numerical study of the run-up generated by three-dimensional landslides. J Geophys Res 110:C03006. doi:10.1029/2004JC002443

Ma G, Shi F, Kirby JT (2012) Shock-capturing non-hydrostatic model for fully dispersive surface wave processes. Ocean Model 43–44:22–35

Ma G, Kirby JT, Shi F (2013) Numerical simulation of tsunami waves generated by deformable submarine landslides. Ocean Model 69:146–165

Ma G, Kirby JT, Hsu TJ, Shi F (2015) A two-layer granular landslide model for tsunami wave generation: theory and computation. Ocean Model 93:40–55

Maeno F, Imamura F (2011) Tsunami generation by a rapid entrance of pyroclastic flow into the sea during the 1883 Krakatau eruption, Indonesia. J Geophys Res 116(B9)

McFall BC, Fritz HM (2016) Physical modeling of tsunamis generated by three-dimensional deformable granular landslides on planar and conical island slopes. Proc R Soc Lond A 472(2188):20160052
McMurtry GM, Tappin DR, Sedwick PN, Wilkinson I, Fietzke J, Sellwood B (2007) Elevated marine deposits in Bermuda record a late quaternary megatsunami. Sediment Geol 200(3–4):155–165. doi:10.1016/j.sedgeo.2006.10.009
Mendoza CI, Santamara-Holek I (2009) The rheology of hard sphere suspensions at arbitrary volume fractions: an improved differential viscosity model. J Chem Phys 130(4):044904. doi:10.1063/1.3063120
Mohammed F, Fritz HM (2012) Physical modeling of tsunami generated by three-dimensional deformable granular landslides. J Geophys Res 117:C11015
Moore JG, Clague DA, Holcomb RT, Lipman PW, Normark WR, Torresan ME (1989) Prodigious submarine landslides on the Hawaiian Ridge. J Geophys Res 94:17,465–17,484
Mueller S, Llewellin EW, Mader HM (2010) The rheology of suspensions of solid particles. Proc R Soc Lond A466(2116):1201–1228. doi:10.1098/rspa.2009.0445
Murty TS (1979) Submarine slide-generated water waves in Kitimat Inlet, British Columbia. J Geophys Res 84(C12):7,777–7,77
Najafi-Jilani A, Ataie-Ashtiani B (2008) Estimation of near-field characteristics of tsunami generation by submarine landslide. Ocean Eng 35(5–6):545–557. doi:10.1016/j.oceaneng.2007.11.006
Okada Y (1985) Surface deformation due to shear and tensile faults in a half space. Bull Seismol Soc Am 75(4):1135–1154
Piper DJW, Cochonat P, Morrison ML (1999) The sequence of events around the epicentre of the 1929 Grand Banks earthquake: initiation of the debris flows and turbidity current inferred from side scan sonar. Sedimentology 46:79–97
Prior DP, Doyle EH, Neurauter T (1986) The Currituck Slide, Mid Atlantic continental slope-revisited. Mar Geol 73:25–45
Quemada D (1977) Rheology of concentrated disperse systems and minimum energy dissipation principle. Rheol Acta 16:82–94. doi:10.1007/BF01516932
Ramalho RS, Winckler G, Madeira J, Helffrich GR, Hiplito A, Quartau R, Adena K, Schaefer JM (2015) Hazard potential of volcanic flank collapses raised by new megatsunami evidence. Sci Adv 1(9):e1500456
Romano F, Piatanesi A, Lorito S, D'Agostino N, Hirata K, Atzori S, Yamazaki Y, Cocco M (2012) Clues from joint inversion of tsunami and geodetic data of the 2011 Tohoku-oki earthquake. Sci Rep 2:385. doi:10.1038/srep00385
Satake K, Fujii Y, Harada T, Namegaya Y (2013) Time and space distribution of coseismic slip of the 2011 Tohoku earthquake as inferred from tsunami waveform data. Bull Seismol Soc Am 103:14731492
Schnyder JSD, Eberli GP, Kirby JT, Shi F, Tehranirad B, Mulder T, Ducassou E, Hebbeln d, Wintersteller P (2016) Tsunamis caused by submarine slope failures along western Great Bahama Bank. Sci Rep (Nature) 6:35925. doi:10.1038/srep35925
Shelby M, Grilli ST, Grilli AR (2016) Tsunami hazard assessment in the Hudson River Estuary based on dynamic tsunami tide simulations. Pure Appl Geophys. doi:10.1007/s00024-016-1315-y
Shi F, Kirby JT, Harris JC, Geiman JD, Grilli ST (2012) A high-order adaptive time-stepping TVD solver for Boussinesq modeling of breaking waves and coastal inundation. Ocean Model 43–44:36–51. doi:10.1016/j.ocemod.2011.12.004
Song C, Wang P, Makse HA (2008) A phase diagram for jammed matter. Nature 453(7195):629632. doi:10.1038/nature06981
Tappin DR, Watts P, McMurtry GM, Lafoy Y, Matsumoto T (2001) The Sissano, Papua New Guinea tsunami of July 1998-offshore evidence on the source mechanism. Mar Geol 175:1–23
Tappin DR, Watts P, Grilli ST (2008) The Papua New Guinea tsunami of 1998: anatomy of a catastrophic event. Nat Hazards Earth Syst Sci 8:243–266
Tappin DR, Grilli ST, Harris JC, Geller RJ, Masterlark T, Kirby JT, Shi F, Ma G, Thingbaijamg KKS, Maig PM (2014) Did a submarine landslide contribute to the 2011 Tohoku tsunami ? Mar Geol 357:344–361. doi:10.1016/j.margeo.2014.09.043
Tehranirad B, Harris JC, Grilli AR, Grilli ST, Abadie S, Kirby JT, Shi F (2015) Far-field tsunami hazard in the north Atlantic basin from large scale flank collapses of the Cumbre Vieja volcano, La Palma. Pure Appl Geophys 172(12):3,589–3,616. doi:10.1007/s00024-015-1135-5
ten Brink U, Twichell D, Geist E, Chaytor J, Locat J, Lee H, Buczkowski B, Barkan R, Solow A, Andrews B, Parsons T, Lynett P, Lin J, and M Sansoucy (2008) Evaluation of tsunami sources with the potential to impact the U.S. Atlantic and Gulf coasts. USGS Administrative report to the U.S. Nuclear Regulatory Commission

ten Brink US, Lee HJ, Geist EL, Twichell D (2009a) Assessment of tsunami hazard to the U.S. East Coast using relationships between submarine landslides and earthquakes. Mar Geol 264:65–73
ten Brink US, Barkan R, Andrews BD, Chaytor JD (2009b) Size distributions and failure initiation of submarine and subaerial landslides. Earth Planet Sci Lett 287:31–42
ten Brink US, Chaytor JD, Geist EL, Brothers DS, Andrews BD (2014) Assessment of tsunami hazard to the U.S. Atlantic margin. Mar Geol 353:31–54
Tinti S, Manucci A, Pagnoni G, Armigliato A, Zaniboni F (2005) The 30th December 2002 landslide-induced tsunami in Stromboli: sequence of the events reconstructed from eyewitness accounts. Nat Hazards Earth Syst Sci 5:763–775
Twichell DC, Chaytor JB, ten Brink US, Buczkowski (2009) Morphology of late quaternary submarine landslides along the U.S. Atlantic Continental Margin. Mar Geol 264:4–15
Viesca RC, Rice JR (2010) Modeling slope instability as shear rupture propagation in a saturated porous medium. In: Mosher DC, Shipp C, Moscardelli L, Chaytor J, Baxter C, Lee HJ, Urgeles R (eds) Submarine mass movements and their consequences IV. Springer, Heidelberg, pp 215–225
Viesca RC, Rice JR (2012) Nucleation of slip-weakening rupture instability in landslides by localized increase of pore pressure. J Geophys Res. doi:10.1029/2011JB008866
Von Huene R, Kirby S, Miller J, Dartnell P (2014) The destructive 1946 Unimak near? Field tsunami: new evidence for a submarine slide source from reprocessed marine geophysical data. Geophys Res Lett 41(19):6811–6818
Viroulet S, Cébron D, Kimmoun O, Kharif C (2013) Shallow water waves generated by subaerial solid landslides. Geophys J Intl 193(2):747–762
Viroulet S, Sauret A, Kimmoun O (2014) Tsunami generated by granular collapse down a rough inclined plane. Eur Phys Lett. doi:10.1209/0295-5075/105/34004
Ward SN, Day S (2001) Cumbre Vieja VolcanoPotential collapse and tsunami at La Palma, Canary Islands. Geophys Res Lett 28:3397–3400. doi:10.1029/2001GL013110
Ward SN, Day S (2003) Ritter Island volcanolateral collapse and the tsunami of 1888. Geophys J Int 154(3):891–902
Watts P and ST Grilli (2003) Underwater landslide shape, motion, deformation, and tsunami generation. In: Proc 13th ISOPE, Honolulu, pp 364–371
Watts P, Grilli ST, Kirby JT, Fryer GJ, Tappin DR (2003) Landslide tsunami case studies using a Boussinesq model and a fully nonlinear tsunami generation model. Nat Hazards Earth Syst Sci 3:391–402
Watts P, Grilli ST, Tappin DR, Fryer G (2005) Tsunami generation by submarine mass failure, II: predictive equations and case studies. J Waterw Port Coast Ocean Eng 131(6):298–310
Wei G, Kirby JT, Grilli ST, Subramanya R (1995) A fully nonlinear Boussinesq model for free surface waves. Part I: highly nonlinear unsteady waves. J Fluid Mech 294:71–92
Wei Y, Newman A, Hayes G, Titov V, Tang L (2014) Tsunami forecast by joint inversion of real-time tsunami waveforms and seismic or GPS Data: application to the Tohoku 2011 tsunami. Pure Appl Geophys 171(12):3281–3305
Weiss R, Fritz HM, Wünnemann K (2009) Hybrid modeling of the mega-tsunami runup in Lituya Bay after half a century. Geophys Res Lett. doi:10.1029/2009GL037814
WRAPUP-2 (2011) Japan quake's economic impact worse than first feared. Reuters, published/accessed 14 April 2011. http://www.reuters.com/article/japan-economy-idUSL3E7FC09220110412
Yavari-Ramshe S, Ataie-Ashtiani B (2015) A rigorous finite volume model to simulate subaerial and submarine landslide generated waves. Landslides. doi:10.1007/s10346-015-0662-6
Yavari-Ramshe S, B Ataie-Ashtiani (2016) Numerical simulation of subaerial and submarine landslide generated tsunami waves - Recent advances and future challenges. Landslides, 44 pps., doi:10.1007/s10346-016-0734-2 (published online 8/3/16)